Crystal Growth and Physical Property Characterization of Complex Perovskite Oxides

A Dissertation Presented for the

Doctor of Philosophy

Degree

The University of Tennessee, Knoxville

Ling Li

August 2015

© by Ling Li, 2015
All Rights Reserved.

To my grandparents Haiqing Li and Xinjie Yi.

Acknowledgments

It has been a precious experience to spend the last five years at University of Tennessee, performing materials research and hiking in the beautiful Great Smoky Mountains. The work presented here would not have been completed without the help of many people I would like to acknowledge here.

I greatly appreciate the support, encouragement and patience from my advisors Prof. Veerle M. Keppens and Prof. David G. Mandrus over the last five years. In particular, I would like to thank Dr. Keppens' for her great help with RUS fits, revising my journal articles and for the extremely helpful Magnetism class! Dr. Mandrus' passion and curiosity for science have always been my inspiration and motivation.

My appreciation goes to Prof. Jiaqiang Yan. I would like to thank him for involving me into the $EuTiO_3$ project, teaching me experimental skills, and for enlightening discussions and guidance. I am also deeply grateful for Prof. Haidong Zhou for sharing his expertise in single crystal growth and experience with PPMS, MPMS with me, and also for fruitful discussions.

I would like to thank Prof. Mariya Zhuravleva for serving on my committee and the time she spent on my dissertation. I thank Prof. T.G. Nieh for the truly encouraging words when I was discouraged by research. I must acknowledge Prof. James R. Morris for the help with Landau theory and more importantly, the best thermodynamics class I have ever taken. I would also like to acknowledge Prof. Wojciech Dmoski for his help with pair distribution analysis.

I also would like to thank all the current and past members in both Keppens lab and Mandrus lab. My special thanks goes to Michael, who taught me a lot of lab skills including RUS fit, LabVIEW, troubleshooting PPMS, etc. I would to thank Lindsay for maintaining the RUS probe, Nirmal and Amal for maintaining multiple instruments in our synthesis lab. I also want to thank you all for the friendship.

I am fortunate to meet so many great friends in Knoxville. I would cherish those potluck/hotpot parties and jokes we shared. Thank you all for being part of my Ph.D. life and bringing so much happiness.

Finally, I would like to thank my parents and all the family members for their unwavering support, love, understanding, and patience that I could never repay.

Life is not easy for any of us. But what of that? We must have perseverance and above all confidence in ourselves. We must believe that we are gifted for something, and that this thing, at whatever cost, must be attained. - Marie Curie

Abstract

Bulk $EuTiO_3$ [europium titanate], a quantum paraelectric antiferromagnet, is shown to exhibit multiferroic behavior in strained thin film form, which highlights the spin-phonon coupling in this system. We have investigated the structural, elastic, magnetic, thermal and transport properties of single crystals of $EuTiO_3$ as well as doped system $EuTi_{1-x}B_xO_3$ (B = Zr, Nb) [Zr and Nb doped europium titanate] utilizing various experimental techniques and theoretical calculations.

The cubic to tetragonal structural transition in pure $EuTiO_3$ is characterized by a pronounced step-like softening of the elastic moduli near 288 K [kelvin], which resembles that of $SrTiO_3$ [strontium titanate] and can be adequately modeled using the Landau free energy model employing the same coupling between strain and octahedral tilting order parameter as previously used to model $SrTiO_3$. Zr doping pushes the antiferromagnetic transition to lower temperatures while maintaining the insulating behavior. Intriguingly, Nb doping shifts the structural phase transition in $EuTiO_3$ to higher temperatures, accompanied by a weakening of octahedral tilting. Furthermore, Nb doping destabilizes the antiferromagnetic ground state of the parent compound and long range ferromagnetic order is observed in the samples containing more than 5% Nb, which is most likely accounted for in terms of the ferromagnetic interaction between localized Eu $4f$ spins mediated by itinerant electrons introduced by Nb doping.

We have also investigated the magnetoelastic coupling effect in $5d$ Re-based double perovskites Ba_2FeReO_6 [barium two iron rhenium oxygen six] and Ca_2FeReO_6

[calcium two iron rhenium oxygen six]. A large softening in C_{44} [shear modulus] over a wide temperature range is observed for Ba_2FeReO_6 below its Curie temperature, which is indicative of a structural distortion. For Ca_2FeReO_6, both the longitudinal and shear modulus show a softening starting at 160 K. In addition, magnetoelastic coupling constants have been estimated from elastic constants and magnetostriction data, which provide direct evidence of pronounced coupling between magnetism and the lattice degrees of freedom present in both compounds.

Table of Contents

1 Introduction **1**

2 Theoretical background **4**

2.1 The geometric tolerance factor 4

2.2 Glazer's notation of octahedral distortion 6

2.3 Magnetism 7

2.3.1 Curie-Weiss Law 9

2.3.2 Exchange Interaction 9

2.3.3 Spin-orbit coupling 11

2.4 Crystal Field Splitting in Perovskites 12

2.5 Landau Free Energy Model 13

3 Experimental Methods **16**

3.1 Sample Synthesis 16

3.1.1 Polycrystalline Samples 16

3.1.2 Single Crystal Growth 16

3.2 X-ray Powder and Laue Diffraction 17

3.3 Thermogravimetric Analysis (TGA) 19

3.4 Magnetization 19

3.5 Electrical Resistivity 20

3.6 Heat Capacity 21

3.6.1 Debye Model 22

3.6.2 Einstein Model . . . 23
3.7 Magnetostriction . . . 24
3.8 Resonant Ultrasound Spectroscopy (RUS) . . . 25
3.8.1 Principle . . . 25
3.8.2 Data collection and analysis . . . 29
3.8.3 Applications to the study of structural phase transitions (SPT) 31

4 Magnetic Phase Diagram of $EuTi_{1-x}B_xO_3$ (B = Zr, Nb) 34
4.1 Introduction . . . 34
4.2 Experimental details . . . 35
4.3 Results . . . 36
4.4 Discussion . . . 43
4.5 Conclusion . . . 44

5 Structural and Magnetic Phase Transitions in $EuTi_{1-x}Nb_xO_3$ 45
5.1 Introduction . . . 46
5.2 Methods . . . 48
5.3 Results . . . 49
5.3.1 X-ray diffraction . . . 49
5.3.2 Magnetization . . . 52
5.3.3 Elastic moduli . . . 52
5.4 Discussion . . . 58
5.4.1 Landau theory . . . 58
5.4.2 Precursor effect . . . 61
5.4.3 Doping Effects . . . 62
5.5 Summary . . . 64

6 Magnetoelastic coupling in A_2FeReO_6 (A = Ba and Ca) probed by elastic constants and magnetostriction measurements 66
6.1 Introduction . . . 67

6.2 Experimental details 68
6.3 Results and Discussion 68
6.4 Summary 74

7 Concluding remarks **75**

Bibliography **77**

Appendix **88**

Vita **91**

List of Tables

2.1 Tolerance factor and glazer notation for common perovskite oxides. . 6

3.1 Measured and fitted resonance frequencies of a $EuTiO_3$ single crystal at 300 K. The last three columns describe the fractional dependence of each mode frequency on each elastic modulus. 30

5.1 Effective moment and Weiss temperature for $EuTi_{1-x}Nb_xO_3$ single crystals derived from Curie - Weiss fits. 52

5.2 T_S, density, and elastic moduli for single crystals of STO, ETO and ETO-Nb. 54

List of Figures

2.1 Ideal cubic ABO_3 perovskite structure with symmetry $Pm\bar{3}m$. A atoms are marked as red and situated at (0 0 0), B atoms are green sitting at (1/2 1/2 1/2) and O atoms are blue sitting at (1/2 1/2 0). 5

2.2 Schematic diagram of the building blocks that result from $a^-a^-c^+$ (left) and $a^-a^-a^-$ (right), respectively. Diagram adapted after Rondinelli & Fennie (2012). 7

2.3 Ordering of the magnetic dipoles in magnetic materials, after Spaldin (2003). 8

2.4 Hysteresis loop of a typical ferromagnet. 9

2.5 Superexchange configuration between two Mn cations, via Oxygen anion. 10

2.6 Double exchange configuration. 11

2.7 (a) Shape of d orbitals, (b) The splitting of e_g and t_{2g} orbitals. 12

2.8 The expected strength of Jahn-Teller effect for octahedral coordination. 13

2.9 Energy *vs.* Q for different α values. 14

3.1 (a) image furnace with feed and seed rods aligned; (b) computer program used to control the growth parameters, also shown is the necking of the melting zone; (c) single crystal $EuTiO_3$ 18

3.2 The Laue pattern of a $EuTiO_3$ single crystal aligned along c axis . . . 18

3.3 Typical TGA measurement demonstrating weight gain vs. time . . . 20

3.4 Diagram of the four probe method for electrical resistivity measurements. 22

3.5 Debye *vs.* Einstein predicted heat capacity as a function of temperature, after Kittle (2005). 24
3.6 (a) The capacitance dilatometer cell inside the custom multifunction probe that can be inserted into the PPMS or Versalab. (b) Schematic drawing of the capacitance dilatometer, after Rotter *et al.* (1998). . . 25
3.7 Home - built RUS probe which can be inserted in a PPMS. 28
3.8 A typical resonance spectrum measured by RUS, after Luan *et al.* (2009) 28
3.9 Typical elastic behavior of a system with no thermodynamic irregularities, after 32
3.10 General behaviour of the elestic modulus C_{ij} at a continuous phase transition. The cases a, b and c are discussed in the text, after Rehwald (1973) 33

4.1 Variation of the lattice parameters with doping concentration x for $EuTi_{1-x}B_xO_3$ (B = Nb, Zr). 37
4.2 Temperature dependence of (a) ZFC susceptibility under 50 Oe and (b) molar heat capacity for $EuTi_{1-x}Zr_xO_3$ ($0 \leq x \leq 1$). The inset of (a) shows the M vs. H curves at 2 K. 38
4.3 Temperature dependence of (a) ZFC susceptibility under 50 Oe and (b) molar heat capacity for $EuTi_{1-x}Nb_xO_3$ ($0 \leq x \leq 1$). The inset of (a) shows the $Mvs.H$ curves at 2 K. 40
4.4 Resistivity *vs.* T for $EuTi_{1-x}Nb_xO_3$ (x = 0.015, 0.2, and 0.4) and $EuTi_{0.97}Zr_{0.03}O_3$. 41
4.5 The magnetic phase diagram of $EuTi_{1-x}Zr_xO_3$ and $EuTi_{1-x}Nb_xO_3$ as determined from magnetic susceptibility measurements. T_C is defined as the maximum point in the plot of dM vs. T. It should be noted that for Nb doping concentration x between 0.1 and 0.16, mixed AFM and FM phases coexist. 42

5.1 Rietveld refinements of the synchrotron X-ray powder patterns of $EuTiO_3$ collected at (a)295 K and (b)100 K respectively. The insets show the (111) and (200) reflections. 50
5.2 (200) peak splitting at 100 K for $EuTi_{1-x}Nb_xO_3$ (x = 0, 0.05, 0.1 and 0.2). 51
5.3 The (200) peak width at 295 K and splitting amplitude at 100 K for $EuTi_{1-x}Nb_xO_3$. 51
5.4 Temperature dependence of *dc* susceptibility for single crystals of $EuTi_{1-x}Nb_xO_3$ (x= 0, 0.05, 0.1, 0.2) in an applied field of 50 Oe. The full and empty symbols denote ZFC and FC data, respectively. . 53
5.5 Temperature dependence of the shear modulus C_{44} and the inverse of the quality factor Q, which is defined as the center frequency of the resonance divided by full width at half maximum, of an oriented ETO single crystal. Note that below the structural phase transition temperature, C_{44} is determined directly from the first resonance peak (the red circle). 55
5.6 Temperature dependence of elastic constants for single crystal $EuTi_{1-x}Nb_xO_3$ (x=0, 0.05, and 0.1) in different magnetic fields. Measurements were performed during cooling. 56
5.7 Temperature dependence of the shear modulus C_{44} for polycrystalline $EuTi_{1-x}Nb_xO_3$ (x=0, 0.03, 0.05, 0.1, 0.2, and 0.3). Data are shifted for clarity. Measurements were performed during cooling. 57
5.8 Temperature dependence of shear modulus C_{44} for single crystal $EuTi_{1-x}Zr_xO_3$ (x=0, 0.005, and 0.015). Measurements were performed during cooling. 58
5.9 The temperature of the structural and magnetic phase transition *vs.* Nb content x in $EuTi_{1-x}Nb_xO_3$. 63

6.1 Temperature dependence of (a) *dc* magnetization at 0.1 T, (b) shear modulus C_{44} at different magnetic fields, and (c) longitudinal modulus C_{11} at different magnetic fields for polycrystalline Ba_2FeReO_6. RUS measurements were performed during cooling. 69

6.2 Temperature dependence of (a) *dc* magnetization at 0.1 T, (b) longitudinal modulus C_{11} and shear modulus C_{44} at differnet magnetic fields for polycrystalline Ca_2FeReO_6. RUS measurements were performed during cooling. 70

6.3 Variation of anisotropic magnetostriction λ_t with magnetic field H at different temperatures for (a) Ba_2FeReO_6 and (b) Ca_2FeReO_6. The insets present λ_t vs. T at 3 Tesla for each compound. 71

6.4 Temperature dependence of the magnetoeleastic coupling constant b for Ba_2FeReO_6 and Ca_2FeReO_6. 72

Chapter 1

Introduction

Multiferroic materials that exhibit strong coupling between electrical, lattice, and magnetic degrees of freedom have generated substantial interest in the past decades. In particular, perovskite oxides (ABO_3) consisting of corner sharing oxygen octahedra provide an excellent platform to investigate the complicated interplay between these freedoms, due to their simple crystal structure and the opportunity for incorporating versatile chemical combinations on the A and B sites. Furthermore, the tilting of the oxygen octahedra in cubic perovskites is known to induce structural phase transitions, which are frequently associated with the emergence of intriguing physical phenomena. In this dissertation, we explore the intricate interplay between magnetism, electrical polarization and lattice in $EuTiO_3$ based perovskites and $5d$ Re-based double perovskites, in the spirit of searching for novel multiferroics that could be applied to multifunctional spintronic devices.

Resonant ultrasound spectroscopy (RUS) is a technique developed by Migliori *et al.* Migliori *et al.* (1993) for determining the complete elastic tensor of a small single crystal by measuring its free-body resonances. It has been proven to be the most sensitive probe to study structural phase transitions driven by soft phonon modes, due to the coupling between strain and the soft modes order parameter. This is effectively demonstrated in the study of $SrTiO_3$, which undergoes an extremely subtle

cubic - to tetragonal distortion at $T_S \approx 105$ K, but exhibits a remarkable change in the temperature dependence of the elastic constants near T_S Bell & Rupprecht (1963a). $EuTiO_3$ is isostructural to $SrTiO_3$ with the addition of a magnetic moment on the Eu-site. Bulk $EuTiO_3$ is a quantum paraelectric antiferromagnet with $T_N \approx 5.6$ K, and exhibits a magnetoelectric coupling as revealed in a decrease of the dielectric constant near T_N Katsufuji & Takagi (2001). More intriguingly, in thin film form with +1.1 % biaxial extension on a $DyScO_3$ substrate, $EuTiO_3$ is shown to exhibit a simultaneous ferroelectric and ferromagnetic ordering Lee *et al.* (2010). This observation highlights the delicate balance between para- and ferroelectricity and between antiferro- and ferromagnetism, and signals the importance of spin - phonon coupling in this system. All these fascinating results motivate us to study the possible structural phase transition in $EuTiO_3$ utilizing RUS, and to examine the intricate balance between electrical and magnetic ordering via physical property measurement system (PPMS) and magnetic property measurement system (MPMS). Note that the properties of perovskites can be readily tuned by chemical substituting (chemical pressure), and in this dissertation we substitute Ti with Zr and Nb. According to the Shannon table Shannon (1976), the radii of Nb^{4+} ($r = 0.68$ Å) and Zr^{4+} ($r = 0.72$ Å) are both greater than that of Ti^{4+} ($r = 0.605$ Å), the difference between these two doping elements lies in their valence states. While both Ti^{4+} and Zr^{4+} hold d^0 configuration in the outer shell, Nb^{4+} has d^1 configuration. Therefore, the proposed investigation would allow one to compare the effect of chemical pressure and electron doping on the structural phase transition and magnetic ground state of the parent compound $EuTiO_3$. Here, laboratory and synchrotron X-ray diffraction and resonant ultrasound spectroscopy (RUS) measurements at various temperatures are employed as the tool to probe structural instabilities, and physical property measurements are carried out as a function of temperature (2-300 K) and magnetic field (0-9 Tesla) using PPMS and MPMS.

Re-based double perovskites $A_2BB'O_6$ (B = $3d$ transition metal, B' = Re) have generated intense interest due to their high Curie temperature and high spin

polarization, making them attractive candidates for industrial applications, see review article Serrate *et al.* (2007). Among them, Sr_2CrReO_6 is shown to possess the highest $T_C \approx 635$ K Kato *et al.* (2002b). From the fundamental research point of view, the strong spin-orbit coupling and unevenly occupied t_{2g} orbitals of $5d$ Re frequently result in the emergence of simultaneous structural, orbital and magnetic ordering. In this work, we synthesized polycrystalline samples of Ba_2FeReO_6 and Ca_2FeReO_6 via solid state reaction, plasma sintered the powder samples, and investigated the magnetoelastic coupling effect in both compounds via elastic constants and magnetostriction measurements.

This dissertation consists of 7 chapters. Chapter 1 briefly introduces the background and our motivation, methods. Chapter 2 discusses the theoretical background and physics that will be used in later chapters. Chapter 3 reviews the main experimental techniques used in this dissertation. Chapter 4 presents the magnetic phase diagram of $EuTi_{1-x}B_xO_3$ (B=Zr and Nb), constructed through results from XRD, *dc* magnetic susceptibility, heat capacity, and electrical resistivity measurements. In Chapter 5, we present resonant ultrasound spectroscopy studies on single crystals of $EuTi_{1-x}B_xO_3$ (B=Zr and Nb) and discuss the interplay between magnetic and lattice degrees of freedom in this system. In Chapter 6, we present investigation of the magnetoelastic coupling in double perovskites Ba_2FeReO_6 and Ca_2FeReO_6 probed by elastic constants and magnetostriction measurements. Concluding remarks will be presented in Chapter 7.

Chapter 2

Theoretical background

In this chapter, we discuss concepts and physics that will be used in later chapters.

2.1 The geometric tolerance factor

Figure 2.1 shows the structure of an ideal ABX_3 perovskite. A perovskite structure is characterized by alternating corner sharing oxygen octahedra (BX_6), whereby A atoms occupy the twelve - coordinate corners of the cubic cells, B atoms are situated in six - coordinate body centers and X atoms are situated in the face centers. However, the structure of most perovskites compounds deviates from cubic symmetry as a result of octahedral rotations. The well known Goldschmidt's tolerance factor t allows for an estimate of the magnitude of the octahedral rotation. It describes the size mismatch between A and B ions:

$$t = \frac{r_A + r_X}{\sqrt{2}(r_B + r_X)} \tag{2.1}$$

where r_A, r_B, and r_X are the ionic radii of A, B and X, respectively. Empirically, if $0.9 \leq t \leq 1$, the structure is undistorted and remains cubic, and distortions occur when t deviates from unity. These distortions manifest themselves as the tilting of

the octahedra to balance the bond length and therefore lower the free energy of the system. There are mainly two situations:

1) if $t > 1$, the A ion is too big and the B ion is too small, which results in a hexagonal structure, such as $BaNiO_3$.

2) if $t < 0.9$, the A ion is too small and the B ion is too big, which results in a orthorhombic/rhombohedral structure, such as $CaTiO_3$ and $GdFeO_3$.

Table 2.1 presents Goldschmidt's tolerance factors for common perovskite oxides. The ionic radii are taken from Shannon's table Shannon (1976). It should be noted that perovskites are not truly ionic compounds therefore the radii adopted may

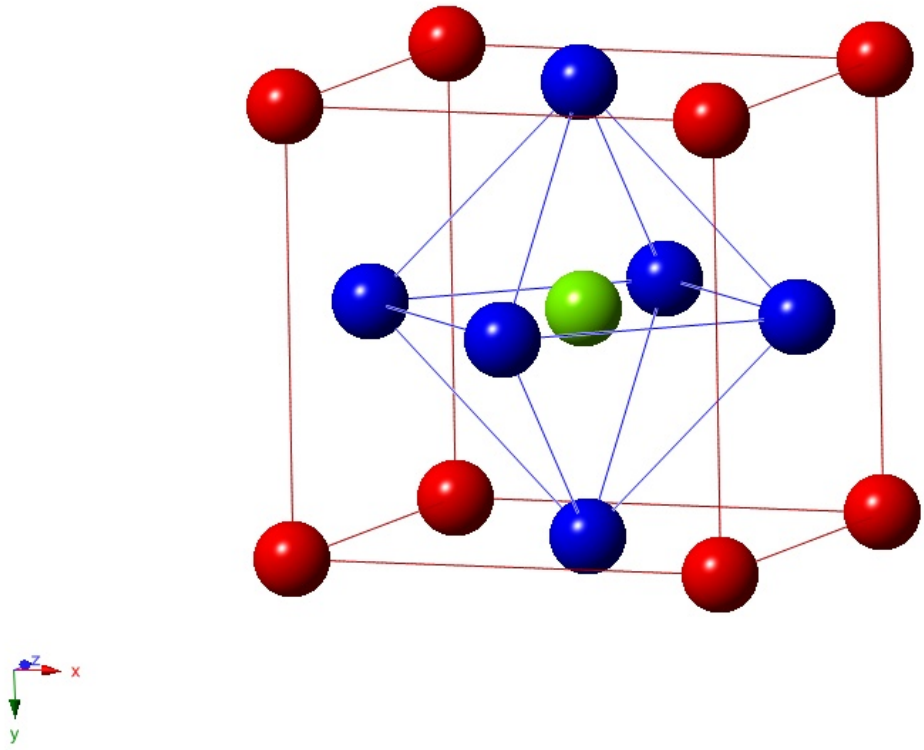

Figure 2.1: Ideal cubic ABO_3 perovskite structure with symmetry $Pm\bar{3}m$. A atoms are marked as red and situated at (0 0 0), B atoms are green sitting at (1/2 1/2 1/2) and O atoms are blue sitting at (1/2 1/2 0).

deviate from those reported in Shannon's table. Given that t values depend heavily on r, the t values shown here are only estimates.

Table 2.1: Tolerance factor and glazer notation for common perovskite oxides.

Composition	t	Space Group	Tilt System
$SrTiO_3$	1	$Pm\bar{3}m$	$a^0a^0a^0$
$BaTiO_3$	1.062	$P4mm$	$a^0a^0c^0$
$CaTiO_3$	0.966	$Pnma$	$a^+b^-b^-$
$PbTiO_3$	1.026	$Pm\bar{3}m$	$a^0a^0c^0$
$NaTaO_3$	0.974	$Pnma$	$a^+b^-b^-$

2.2 Glazer's notation of octahedral distortion

When the mismatch between A and B ions in a ABO_3 perovskite causes oxygen octahedra to tilt in some particular way, it causes the tilting of the neighboring octahedra in the extended framework. Glazer developed a useful notation in 1972 to describe octahedra tilting distortions in perovskites Glazer (1972), which considers the tilting about any of the high symmetry axes. The Glazer's notation for common perovskties are also given in Table 2.1. In this classification scheme, three letters are accompanied by a superscript of 0, + or - . The three letters correspond to the x, y, and z axis of the perovskite structure and identical letters indicate the same amplitude of tilt. The superscripts + and - indicate whether the tilting between adjacent layers are in the same (in phase) or opposite (out of phase) directions. A superscript of 0 is used when a given structure does not display any tilting. For example, $a^+b^-b^-$ denotes tilting for $Pnma$ perovskites, which consists of in phase tilting about the x axis and out of phase tilting about y and z axes. It also indicates that the tilts about y and z axes have equal magnitude. Figure 2.2 presents a schematic diagram of the building blocks that result from $a^-a^-c^+$ and $a^-a^-a^-$, respectively.

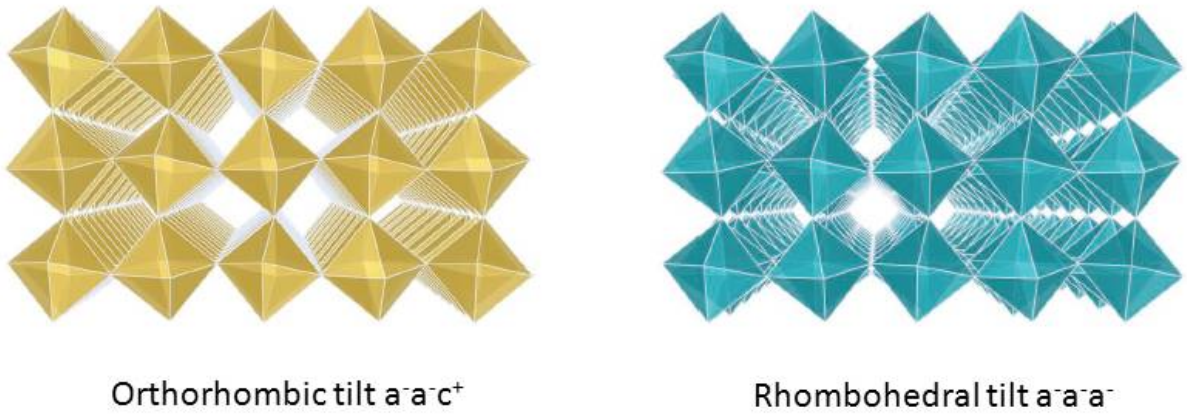

Figure 2.2: Schematic diagram of the building blocks that result from $a^-a^-c^+$ (left) and $a^-a^-a^-$ (right), respectively. Diagram adapted after Rondinelli & Fennie (2012).

2.3 Magnetism

Magnetism is originated from unpaired electrons in the outer shell and their interactions with each other. The magnetic moment of a free atom in the absence of a magnetic field consists of two contributions: the orbital angular momentum and the spin angular momentum. The solution of the Schrodinger equation leads to the quantization of the orbital momentum of the electrons. Each electron is characterized by four quantum numbers: n, l, m_l, and m_s. n and l are called the principle and angular momentum quantum numbers, and m_l and m_s are called the magnetic and spin quantum numbers. The magnetic susceptibility is defined as the ratio of M to H:

$$\chi = \frac{M}{H}(\frac{emu}{mol.Oe}) \tag{2.2}$$

where M is the magnetization and H is the magnetic field applied. The susceptibility indicates how responsive a material is to an applied magnetic field.

As shown in Figure 2.3, magnetic materials can be classified into several groups (para-, antiferro-, ferro- and ferrimagnet) according to how the local atomic moments interact with each other. The individual atomic moments of a paramagnet are

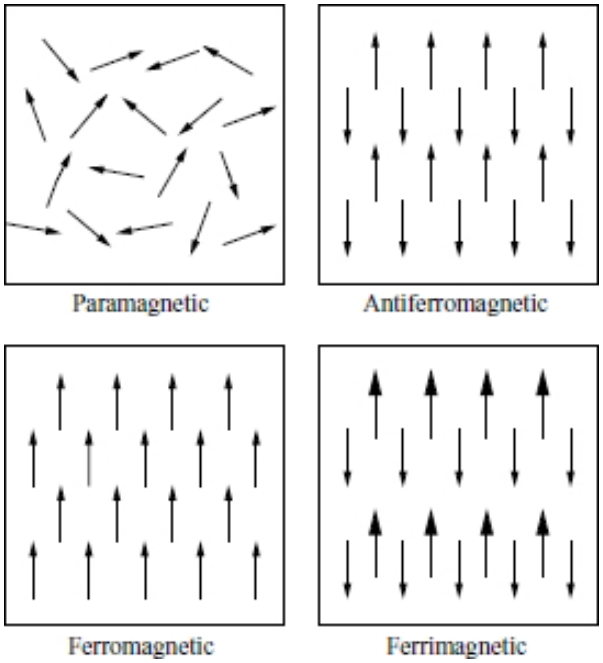

Figure 2.3: Ordering of the magnetic dipoles in magnetic materials, after Spaldin (2003).

randomly aligned thus the total moments sum to zero. Conversely, the latter three magnetic materials are characterized by ordered spin moments. Ferromagnetic materials are characterized by the long-range ordering of parallel moments, which exist even in the absence of a magnetic field. However this spontaneous magnetization is observed to vanish above T_C, which is called the Curie temperature. Figure 2.4 shows a typical hysteresis loop of a ferromagnet. An antiferromagnet is characterized by the long-range ordering of antiparallel moments with zero net moment. Lastly, ferrimagnets possess two or multiple antiferromagnetically coupled sublattices with unequal moments. Those sublattices are usually occupied by different elements.

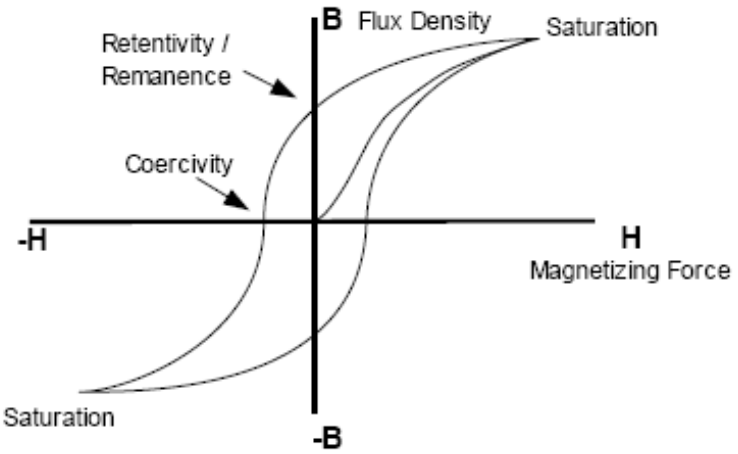

Figure 2.4: Hysteresis loop of a typical ferromagnet.

2.3.1 Curie-Weiss Law

The Curie-Weiss Law describes the magnetic susceptibility χ of a ferri/ferromagnet or antiferromagnet in the paramagnetic region:

$$\chi = \frac{C}{T - T_c} \tag{2.3}$$

where T is the absolute temperature in Kelvin, and C is the Curie constant. A general approach to obtain μ_{eff} and the Curie-Weiss temperature θ_{CW} is to fit $1/\chi$ *vs.* T in the paramagnetic region to a linear function.

2.3.2 Exchange Interaction

The exchange interaction is a quantum mechanical effect between identical particles. The Heisenberg Hamiltonian for a single pair of spins:

$$H = -2JS_1 \cdot S_2 \tag{2.4}$$

$J > 0$ indicates a ferromagnetic interaction, favoring $\uparrow\uparrow$ alignment.

$J < 0$ indicates an antiferromagnetic interaction, favoring $\uparrow\downarrow$ alignment.

Here, the interaction represented by equation 2.4 does not require an intermediatory and is called a direct exchange interaction. Besides this direct exchange mechanisms, there also exists some interactions that take place even when there is no direct overlap of the electronic wave functions on magnetic ions. These include superexchange interaction, double exchange interaction, Ruderman-Kittel-Kasuya-Yosida (RKKY) interaction, and anisotropic exchange interaction like the Dzyaloshinskii- Moriya interaction for noncentrosymmetric materials. This dissertation is concerned with the first three kinds, which will be reviewed briefly in the following paragraph.

Superexchange

Superexchange is an indirect interaction between two magnetic cations, via an intervening anion, often O^{2-} ($2p^6$). It is a short range interaction, which could result in both FM and AFM ordering.

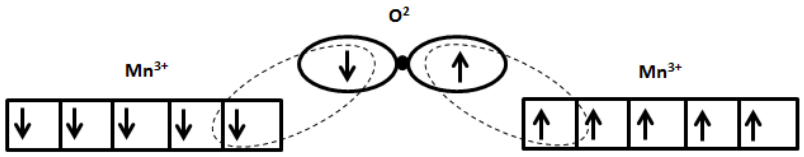

Figure 2.5: Superexchange configuration between two Mn cations, via Oxygen anion.

Double Exchange

Double exchange refers to a type of magnetic interaction between ions in different oxidation states, as shown in Figure 2.6. It can lead to spin canting if existing in an antiferromagnetically ordered lattice.

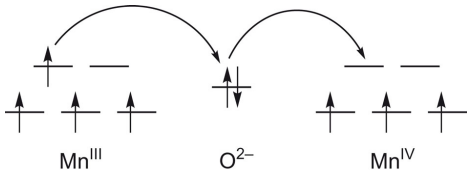

Figure 2.6: Double exchange configuration.

RKKY interaction

RKKY interaction refers to the magnetic exchange interaction between localized d or f moments mediated by itinerant electrons. The theory to describe exchange interaction is based on Bloch wavefunctions:

$$H(R_{ij}) = \frac{I_i \cdot I_j}{4} \frac{|\Delta k_m k_m|^2 \, m^*}{(2\pi)^3 R_{ij}^4 \hbar^2} [2k_m R_{ij} cos(2k_m R_{ij}) - sin(2k_m R_{ij})] \tag{2.5}$$

where H is the Hamiltonian, R_{ij} is the distance between the nuclei i and j, I_i is the nuclear spin of atom i, $\Delta k_m k_m$ is a term that represents the strength of the hyperfine interaction, m^* is the effective mass of the electrons in the crystal, and k_m is the wave vector of the conduction electrons. RKKY usually leads to long range magnetic ordering, that can be ferromgnetic or antiferomagnetic in nature.

2.3.3 Spin-orbit coupling

Spin-orbit coupling occurs when the magnetic moment from the electron's spin interacts with the magnetic field from its orbital motion. Because the magnitude of spin-orbit coupling is proportional to Z^4, it exists mainly in heavy $4d$ and $5d$ elements like Ir, Re, and Os, etc. Spin-orbit coupling results in the emergence of interesting physical phenomena like magneto-elastic coupling, and has been the heart of fundamental research for years.

2.4 Crystal Field Splitting in Perovskites

Crystal Field Theory (CFT) describes the breaking of degeneracies of electron orbital states, usually d or f orbitals. This effect arises from a static electric field produced by a surrounding charge distribution (anion neighbors). The most common complexes are octahedral and tetragonal. In perovskite oxides, the transition metal cations are in octahedral environments. Figure 2.7(a) shows the shape and orientations of the d orbitals. By convention, the d_{xy}, d_{yz} and d_{xz} orbitals in a octahedral complex are called the t_{2g} orbitals, while $d_{x^2-y^2}$ and d_{z^2} are called e_g orbitals. The lobes of the three t_{2g} orbitals lie between the O^{2-} ions, while the lobes of the two e_g orbitals point towards the O^{2-} ions. In a free d ion, all the five orbitals have the same energy therefore degenerate. Interestingly, e_g and t_{2g} orbitals are influenced differently when the ligands (O^{2-}) are brought closer to the orbitals when octahedral tilting is present. As a consequence, the orbital degeneracies are partly removed, as shown in Figure 2.7(b). The three t_{2g} orbitals have lower energy than the e_g orbitals.

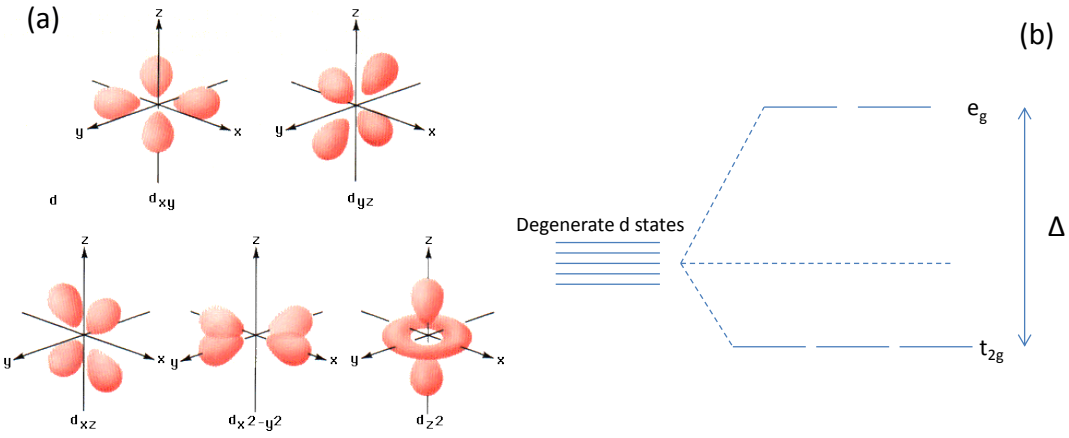

Figure 2.7: (a) Shape of d orbitals, (b) The splitting of e_g and t_{2g} orbitals.

The well-known Jahn-Teller effect or Jahn-Teller distortion refers to the geometric distortion of molecules and ions in an octahedral complex to remove orbital degeneracy. This electronic effect is named after Hermann Arthur Jahn and Edward

Teller, who proved, using group theory, that orbital nonlinear spatially degenerate molecules cannot be stable Jahn & Teller (1937). This effect is most pronounced when the e_g orbitals are unevenly occupied. Figure 2.8 shows the expected strength of the Jahn-Teller effect for ions with different electron configurations in a octahedral complex.

Jahn－Teller effect

Number of d electrons	1	2	3	4		5		6		7		8	9	10
High/Low Spin				HS	LS	HS	LS	HS	LS	HS	LS			
Strength of J-T Effect	w	w		s	w		w	w		w	s		s	

Figure 2.8: The expected strength of Jahn-Teller effect for octahedral coordination.

Here w means weak (t_{2g} orbitals unevenly occupied), s means strong (e_g orbitals unevenly occupied) and blank means no JT effect.

2.5 Landau Free Energy Model

Landau model is a general approach to study phase transitions. In the vicinity of a second order phase transition, the order parameter increases continuously from zero starting at the critical temperature. The free energy can be written as a Taylor expansion in terms of the order parameter Q

$$f(T) = f_0(T) + \alpha Q^2 + \frac{\beta}{2} Q^4 + ... \tag{2.6}$$

Here, Q is the order parameter, α and β are parameters, and $f_0(T)$ describes the temperature dependence of the high temperature phase near the phase transition. At the critical temperature, the free energy is minimized ($\frac{\partial f}{\partial Q} = 0$), yielding:

$$2\alpha Q + 2\beta Q^3 = 0 \Rightarrow Q = 0 or Q^2 = -\frac{\alpha}{\beta} \tag{2.7}$$

The transition occurs when α changes sign, therefore we assume the temperature dependence of α as

$$\alpha(T) = \alpha_0(T - T_C), \alpha_0 > 0 \tag{2.8}$$

It is assumed that $\beta > 0$, so that the free energy has a minimum for finite values of the order parameter. When $\alpha > 0$, there is only one minimum at $Q = 0$ (the high temperature phase). When $\alpha < 0$, there are two minima with $Q \neq 0$, as shown in Figure 2.8.

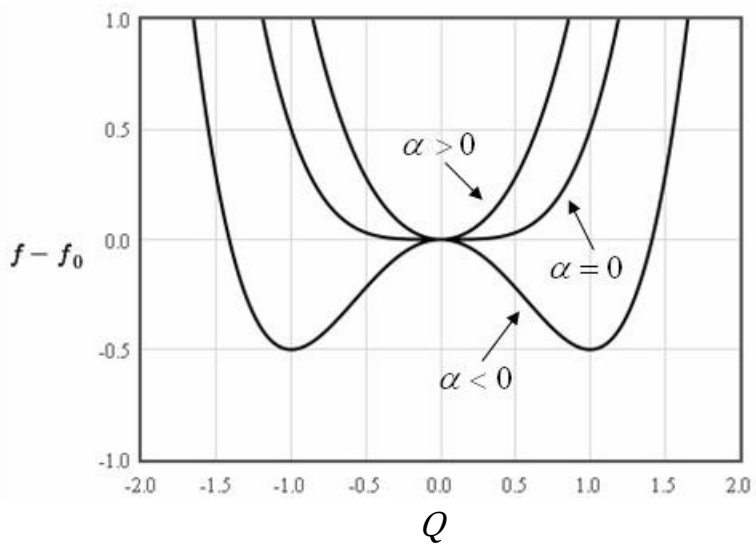

Figure 2.9: Energy *vs.* Q for different α values.

Landau theory is frequently used in the study of second order structural phase transitions, whereby the free energy f is written as

$$f = f(e) + f(Q) + f(Q, e) \tag{2.9}$$

where $f(e)$ is the elastic energy, $f(Q)$ is the energy resulted from the order parameter change in the vicinity of the transition and $f(Q, e)$ is the additional part

arising from the coupling between strain and order parameter. We will discuss the application of Landau theory to the study of SPT in detail in Chapter 5.

Chapter 3

Experimental Methods

3.1 Sample Synthesis

3.1.1 Polycrystalline Samples

Polycrystalline samples are prepared via a standard solid state reaction method. Stoichiometric mixtures of high-purity (at least 99.99 %) starting materials from Alfa Aesar are mixed and ground in an agate mortar and then pressed into pellets. For the $EuTi_{1-x}B_xO_3$ (B = Zr and Nb) system, the pressed pellets are sintered in a MTI tube furnace (Model: GSL1500X) with a flowing 90:10 Ar:H_2 atmosphere at 1300 $\sim$ 1400 °C with intermediate grindings. For A_2FeReO_6 (A = Ba and Ca), the starting materials are mixed and ground in a glove box, and the pellets are calcined in an evacuated sealed quartz tube in a box furnace at 900 °C for 3 hours and 1100 °C for another 3 hours.

3.1.2 Single Crystal Growth

High quality single crystals without grain boundaries and impurities are essential in order to obtain reliable results from physical property measurements. In this dissertation, single crystals of $EuTi_{1-x}Zr_xO_3$ (x = 0, 0.005, 0.015, 0.03) and

$EuTi_{1-x}Nb_xO_3$ (x = 0, 0.05, 0.1 and 0.2) have been grown by the floating zone technique (FZT) in an IR-heated image furnace (NEC) equipped with two 1500 W lamps and double ellipsoidal mirrors. The present system is congruent and the experimental growth procedures for different compositions are similar. Here we describe the details of melting these compounds. Single phase polycrystalline powders are first prepared via a solid state reaction method, as described in the polycrystalline sample preparation section. Then the powders are inserted into a balloon and pressed into rods utilizing a hydrostatic press. The rods (feed and seed) are finally sintered at 1400 °C in 90:10 Ar:H_2 atmosphere to achieve high density. Note that the rods should be as straight/uniform as possible in order to improve the melting process later. As shown in Figure 3.1 (a), the feed rod is suspended using a copper wire and the seed rod is positioned in a ceramic holder on the lower shaft. During the growth, the feed and seed rods are pulled down together with a speed of 10mm/h while rotating in opposite directions at 25 rpm, and the crystals are grown at the solidifying end of the molten zone. Figure 3.1(b) shows the interface of the software we use to control the growth parameters (lamp voltage, lowering rate, rotating rate, etc). Also shown in Figure 3.1(b) is the necking of the molten zone during the crystal growth process. A typical crystal obtained using the floating zone technique is shown in Figure 3.1(c).

The greatest advantage of this technique is that it is contaminate free since no crucible is involved in the growth. Moreover, it allows for crystal growth in different gas atmosphere and under pressure. This technique usually yields bigger crystals than other crystal growth techniques like chemical vapor transport or flux growth.

3.2 X-ray Powder and Laue Diffraction

Powder X-ray diffraction (XRD) patterns were recorded with a HUBER Imaging Plate Guinier Camera 670 with Ge monochromatized $CuK_{\alpha 1}$ radiation (λ = 1.54059$\mathring{A}$). Rietveld refinements were obtained using FullProf Rodrguez-Carvajal (1993), which allows for a determination of the crystal structure and lattice parameters. To better

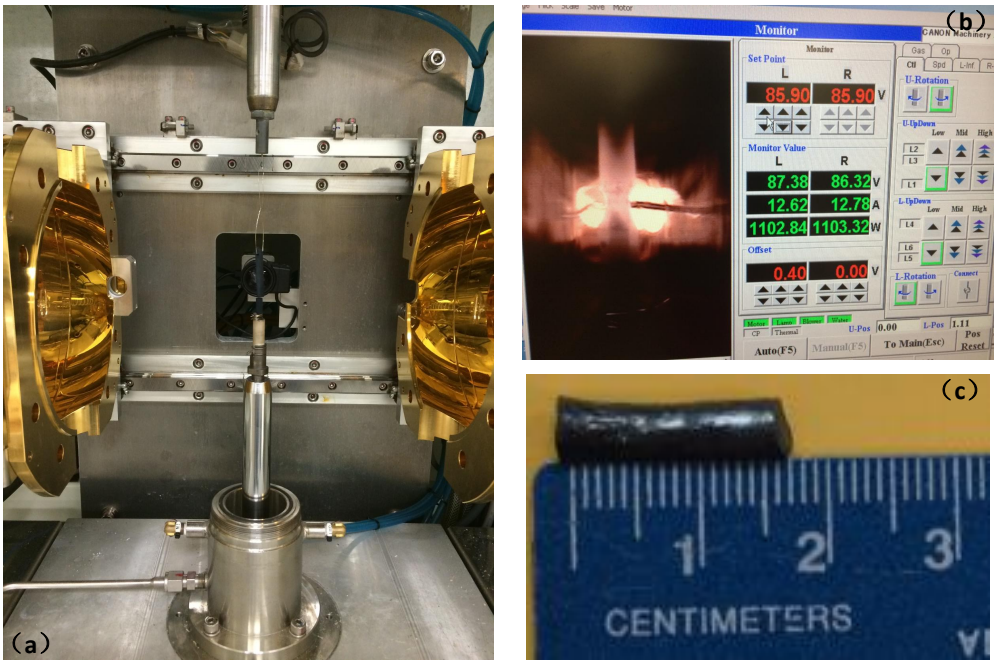

Figure 3.1: (a) image furnace with feed and seed rods aligned; (b) computer program used to control the growth parameters, also shown is the necking of the melting zone; (c) single crystal $EuTiO_3$

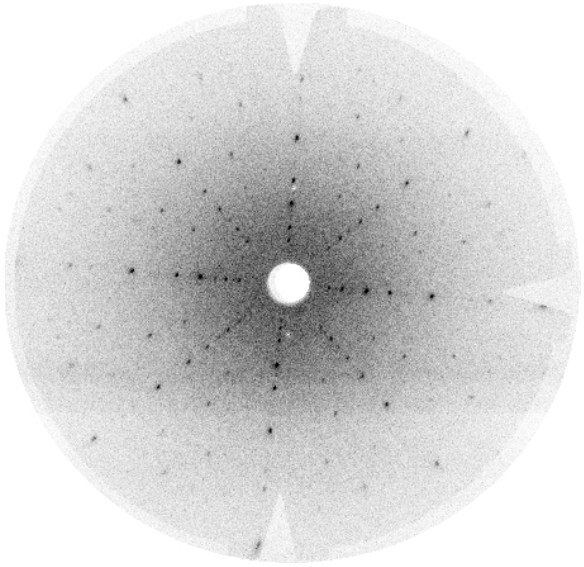

Figure 3.2: The Laue pattern of a $EuTiO_3$ single crystal aligned along c axis

resolve the tetragonal distortion at low temperatures, synchrotron powder XRD was performed at the 11-BM beamline of the Advanced Photon Source at Argonne National Laboratory. Single crystals of $EuTi_{1-x}Nb_xO_3$ ($x = 0$, 0.05, 0.1 and 0.2) were ground to fine powders and loaded in a capillary tube with a diameter of 0.8 mm. The experiments were carried out with a fixed wavelength ($E = 30\ keV$, $\lambda = 0.41396(1)\mathring{A}$) at T = 295 K and 100 K.

X-ray Laue diffraction is used to confirm crystal quality and align the crystals along certain crystallographic direction. Figure 3.2 shows a Laue back scattering pattern of a $EuTiO_3$ single crystal oriented along the c axis. The clear and round spots indicate high crystal quality. OrientExpress is used to align the crystal through fitting the recorded pattern to a simulated pattern.

3.3 Thermogravimetric Analysis (TGA)

A thermogravimetric analyzer (TGA) was used to determine the oxygen content of the samples. Single crystals were ground to fine powders, and heated up to 1000 °C with air gas flowing across the furnace. The oxygen content is determined from the weight gain during the oxidation process from $EuTiO_{3+\delta}$ to $Eu_2Ti_2O_7$. Figure 3.3 shows a typical curve of weight (percentage) gain with time. The mass drops slightly in the beginning due to moisture evaporation. Then it increases with time/temperature and saturates when it is fully oxidized to $Eu_2Ti_2O_7$. Note that the resultant powder was checked using XRD to be pure $Eu_2Ti_2O_7$. For each composition, we repeated the experiment multiple times to get a reliable result.

3.4 Magnetization

The *dc* magnetization experiments are carried out in a Quantum Design Magnetic Property Measurement System (MPMS 3). The MPMS 3 enables measurements in the temperature interval of 1.8 K $\leq$ T $\leq$ 400 K and under a magnetic field up to 7

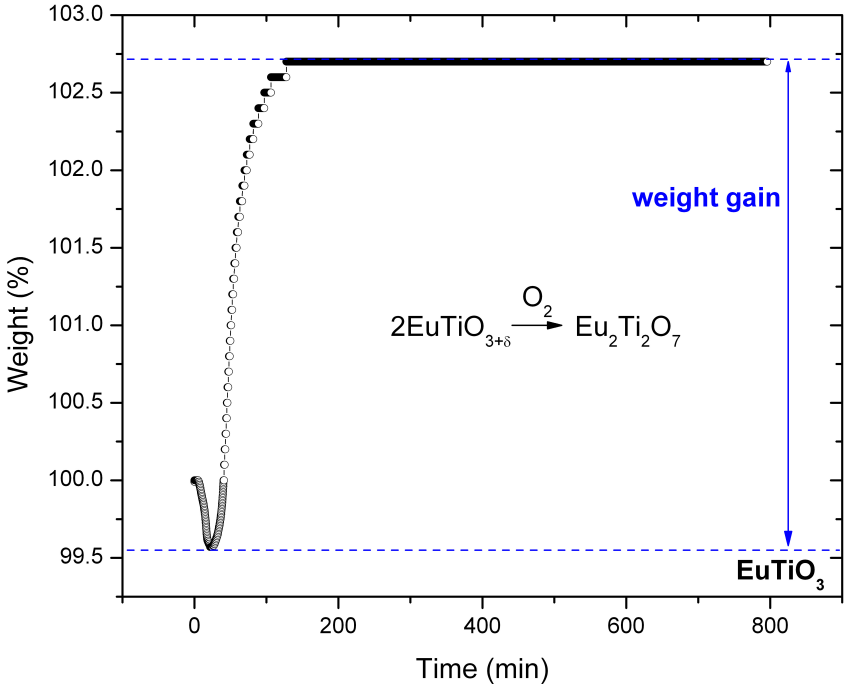

Figure 3.3: Typical TGA measurement demonstrating weight gain vs. time

Tesla. The M *vs.* T measurements are performed while warming up after both zero - field - cooling (ZFC) and field - cooling (FC) conditions.

The MPMS 3 is a liquid helium free EverCool system with SQUID sensitivity. It allows an initial cooling down of the system from helium gas within 30 hours. It also possesses multiple options including AC susceptibility measurements, VSM with oven up to 1000 K, etc.

3.5 Electrical Resistivity

Electrical resistivity is an intrinsic property that quantifies how strongly a given material opposes the flow of electric current. It is not only the direct quantity to classify metal, semiconductor and insulators, it is also one of the most sensitive

approach to probe phase transitions in a material driven by temperature or magnetic field.

Electrical resistivity measurements are carried out in a Quantum Design Physical Properties Measurements System (PPMS) in the temperature interval 2 K$\leq$ T $\leq$300 K in magnetic fields up to 9 Tesla utilizing the four-wire method. Figure 3.4 shows the common set up for a four-wire resistivity measurement. Four gold wires are used to attach a rectangular sample to a sample puck via silver epoxy (leads 1-4). Current is passed via leads 1 and 4, while leads 2 and 3 are used to measure the potential difference. Using Ohm's law and the relation between the measured resistance R and the material's resistivity ρ:

$$R = \rho \frac{L}{A} \tag{3.1}$$

with L the length of the sample and A the cross section area, the accurate resistivity of a sample can be calculated. Typical sample size for a four-wire experiment is 0.5 mm $\times$ 0.5 mm $\times$ 3 mm^3. The advantage of this method is that the voltage leads draw very little current, which allows for an accurate measurement of both the current and voltage drop across the sample.

3.6 Heat Capacity

Heat capacity measurements are also carried out in a Quantum Design PPMS. $C(T) = \frac{\delta Q}{\delta T}$ measures the heat energy transferred to an object and the resulting increase in the temperature of the object. Molar heat capacity has a unit of $C_{mol} = \frac{J}{mol.K}$. In theory, heat capacity can be measured at constant volume C_V or constant pressure C_P. Our measurements are performed under a constant pressure condition. Theoretical, there are two models predicting the temperature dependence of heat capacity.

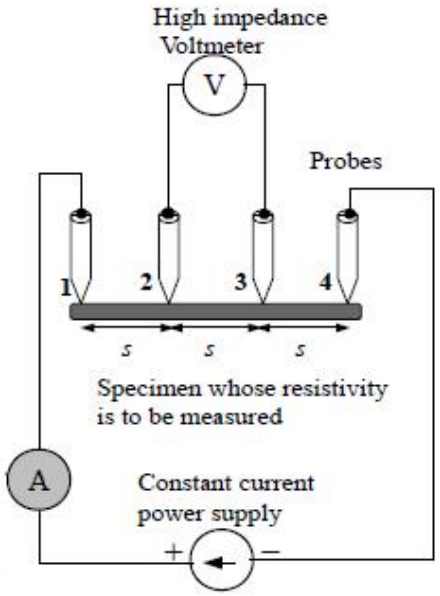

Figure 3.4: Diagram of the four probe method for electrical resistivity measurements.

3.6.1 Debye Model

In the Debye approximation the velocity of sound is taken as constant for each mode, and the dispersion relation is written as

$$\omega = vK \tag{3.2}$$

where v is the sound velocity, and the density of states is given by

$$D(\omega) = V\omega^2/2\pi^2v^3 \tag{3.3}$$

Here only acoustic phonon modes are considered. Assume there are N primitive cells, and the phonon velocity is independent of the polarization, the total thermal energy is given by

$$U = \frac{3V\hbar}{2\pi^2v^3}\int_0^{\omega_D} d\omega \frac{\omega^3}{e^{\frac{\hbar\omega}{\tau}} - 1} = \frac{3Vk_B{}^4T^4}{2\pi^2v^3\hbar^3}\int_0^{x_D} dx \frac{x^3}{e^x - 1} \tag{3.4}$$

where ω_D is the cutoff frequency and

$$x \equiv \hbar\omega/\tau \equiv \hbar\omega/k_B T$$

$$x_D \equiv \hbar\omega_D/k_B T \equiv \theta/T$$

The debye temperature θ may also be expressed as

$$\theta = \frac{\hbar v}{k_B}(\frac{6\pi^2 N}{V})^{1/3} \tag{3.5}$$

The heat capacity is the derivative of total thermal energy U to temperature, it is given as

$$C_V = \frac{3V\hbar^2}{2\pi^2 v^3 k_B T^2}\int_0^{\omega_D} d\omega \frac{\omega^4 e^{\hbar\omega/\tau}}{(e^{\hbar\omega/\tau}-1)^2} = 9Nk_B(\frac{T}{\theta})^3\int_0^{x_D} dx \frac{x^4 e^x}{(e^x-1)^2} \tag{3.6}$$

Debye T^3 Law

At very low temperatures ($T \ll \theta$),

$$C_V \cong \frac{12\pi^4}{5}Nk_B(\frac{T}{\theta})^3 \cong 234Nk_B(\frac{T}{\theta})^3 \tag{3.7}$$

In real systems, this law is only valid at very low temperatures ($T < \frac{\theta}{50}$).

3.6.2 Einstein Model

Consider N oscillators of the same frequency ω_0 and in one dimension. The thermal energy is given

$$U \equiv N\langle n\rangle \hbar\omega = \frac{N\hbar\omega}{e^{\hbar\omega/\tau}-1} \tag{3.8}$$

The heat capacity is given

$$C_V = (\frac{\partial U}{\partial T})_V = Nk_B(\frac{\hbar\omega}{\tau})^2\frac{e^{\hbar\omega/\tau}}{(e^{\hbar\omega/\tau}-1)^2} \tag{3.9}$$

Figure 3.5 shows a comparison of the temperature dependence of the heat capacity predicted by the Debye and Einstein models.

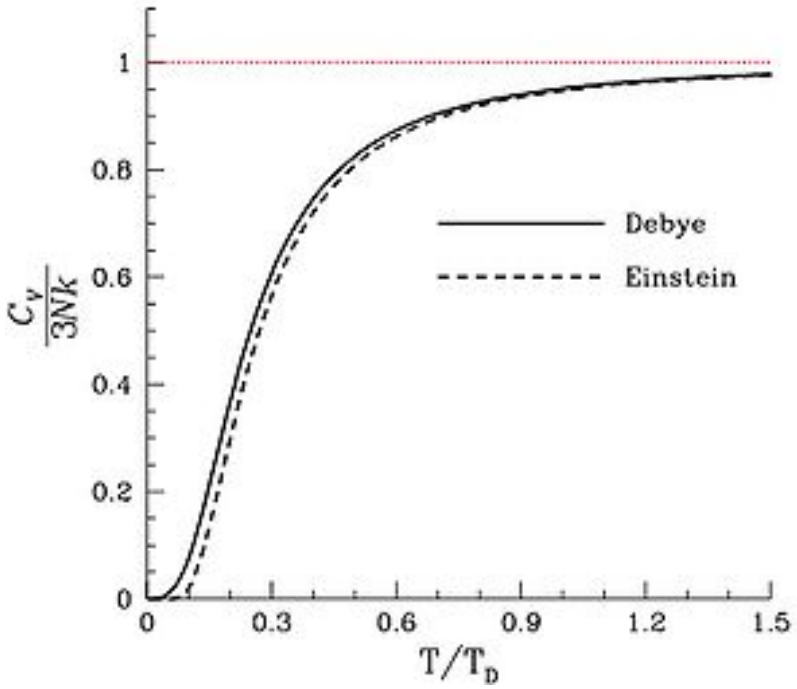

Figure 3.5: Debye *vs.* Einstein predicted heat capacity as a function of temperature, after Kittle (2005).

3.7 Magnetostriction

Magnetostriction is a property of ferromagnetic materials that causes the material to change dimensions during magnetization. The capacitance dilatometer determines the length change from the measurements of the capacitance, which is one of the most sensitive method for measuring small length changes of solids. Not all capacitance dilatometers are created equally. Figure 3.6(a) shows a picture of our capacitance dilatometer cell and (b) shows the schematic drawing of the capacitance dilatometer cell. We chose the capacitive method with tilted plates designed by Rotter *et al.*, whereby the sample is placed in a hole in the lower capacitance plate Rotter *et al.*

(1998). This design reduces the cell volume, which effectively increases the thermal stability. A detailed description of the design can be found in Rotter *et al.* (1998).

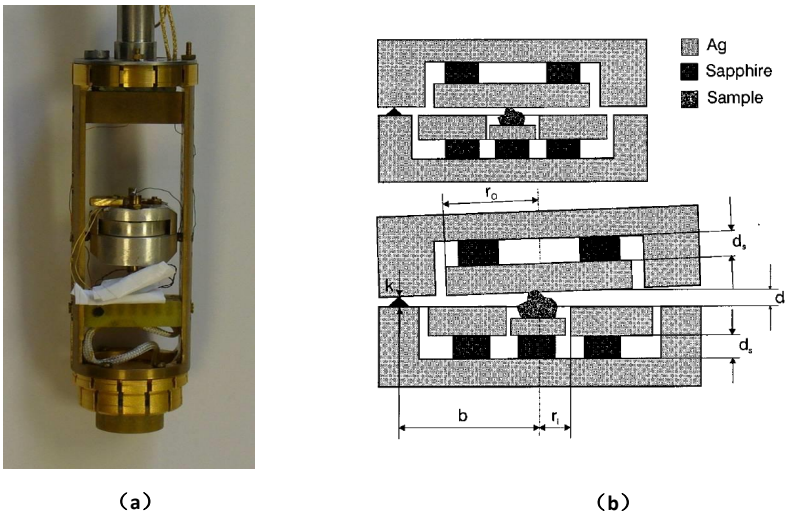

Figure 3.6: (a) The capacitance dilatometer cell inside the custom multifunction probe that can be inserted into the PPMS or Versalab. (b) Schematic drawing of the capacitance dilatometer, after Rotter *et al.* (1998).

3.8 Resonant Ultrasound Spectroscopy (RUS)

3.8.1 Principle

RUS is a technique developed by Migliori *et al.* Migliori *et al.* (1993) for determining the complete elastic tensor of a small single crystal by measuring its free-body resonances. It allows determination of the full elastic tensor without needing to change transducers or remounting the sample. RUS involves two procedures - direct and inverse. The direct procedure computes the resonance frequencies from the elastic moduli, whereas the inverse procedure calculates the elastic moduli from resonance frequencies. Below, we show the computations involved in the fitting procedure.

Lagrangian minimization

For an object with a free surface S surrounding a volume V, the general form of the Lagrangian is as follows,

$$L = \int_V (KE - PE) dV \tag{3.10}$$

where KE and PE are the kinetic energy density and potential energy density, respectively. They can be written as

$$KE = \frac{1}{2} \sum^{i} \rho \omega^2 {u_i}^2 \tag{3.11}$$

Here, u_i is the ith component of the displacement vector, ω is the angular frequency from harmonic time dependence, c_{ijkl} is a component of the elastic tensor, and ρ is the density.

Under the equilibrium conditions, $\frac{\partial L}{\partial u} = 0$. We let u vary arbitrarily in V and on S ($u_i \to u_i + \delta u_i$) and calculate the variation in $L(\delta L)$. The gives

$$L + \delta L = \int_V [\frac{1}{2} \sum_i \rho \omega^2 (u_i + \delta u_i)^2 - \sum_{i,j,k,l} c_{ijkl} \frac{\partial (u_i + \delta u_i)}{\partial x_j} \frac{\partial u_k}{\partial x_l}] \tag{3.12}$$

Keeping terms to first order in δu_i, we find

$$\delta L = \int_V [\sum_i \rho \omega^2 u_i \delta u_i - \sum_{i,j,k,l} c_{ijkl} \frac{\partial (\delta u_i)}{\partial x_j} \frac{\partial u_k}{\partial x_l}] dV \tag{3.13}$$

which, after an integration by parts, yields

$$\delta L = \int_V (\sum_i [\rho \omega^2 u_i + \sum_{j,k,l} c_{ijkl} \frac{\partial^2 u_k}{\partial x_j \partial x_l}] \delta u_i) dV - \int_S (\sum_i [\sum_{j,k,l} \vec{n_j} c_{ijkl} \frac{\partial u_k}{\partial x_l}] \delta u_i) dS \tag{3.14}$$

Because δu_i is arbitrary in V and on S, the values of u_i that correspond to stationary points of L (i.e., $\delta L = 0$) must satisfy the condition that the terms in

square brackets in Equation 3.14 are zero. The first term yields the elastic wave equation:

$$\rho\omega^2 u_i + \sum_{j,k,l} c_{ijkl} \frac{\partial^2 u_k}{\partial x_j \partial x_l} = 0 \tag{3.15}$$

The second terms yields is an expression of free-surface boundary conditions:

$$\sum_{j,k,l} \vec{n_j} c_{ijkl} \frac{\partial u_k}{\partial x_l} = \sum_j \vec{n_j} \sigma ij = 0 \tag{3.16}$$

where σ_{ij} is the ij th component of the stress tensor. The set of u_i that satisfies the above conditions are precisely those displacements that correspond to ω being a normal mode frequency of the system. Using the Rayleigh-Ritz method, we expand the displacement vector u_i in a complete set of basis functions, substituting that expression into Equation 3.10 and finding the stationary points of the Lagrangian which then yields an eigenvalue problem that can be readily solved, namely

$$\omega^2 \vec{E}\vec{a} = \Gamma\vec{a} \tag{3.17}$$

Equation 3.17 determines the resonance frequencies from the elastic moduli. Migliori and co-workers have coded the so-called inverse problem to extract elastic tensor from resonance frequencies. It should be noted that good initial guesses of elastic moduli are of essential importance to obtain a good fit.

The advantages of RUS can be summarized as follows:

1. It works for very small crystals with symmetry as low as Orthorhombic.
2. It is nondestructive, the samples could be reused for other measurements.
3. All components of the elastic tensor can be determined simultaneously to very high accuracy, without needing to change transducers or remounting the sample.

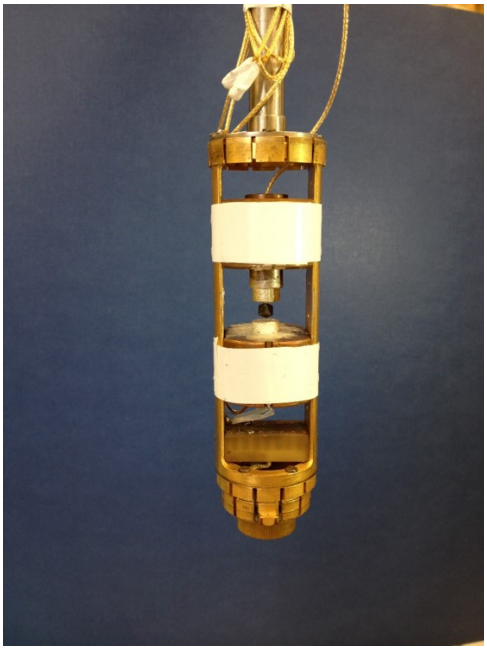

Figure 3.7: Home - built RUS probe which can be inserted in a PPMS.

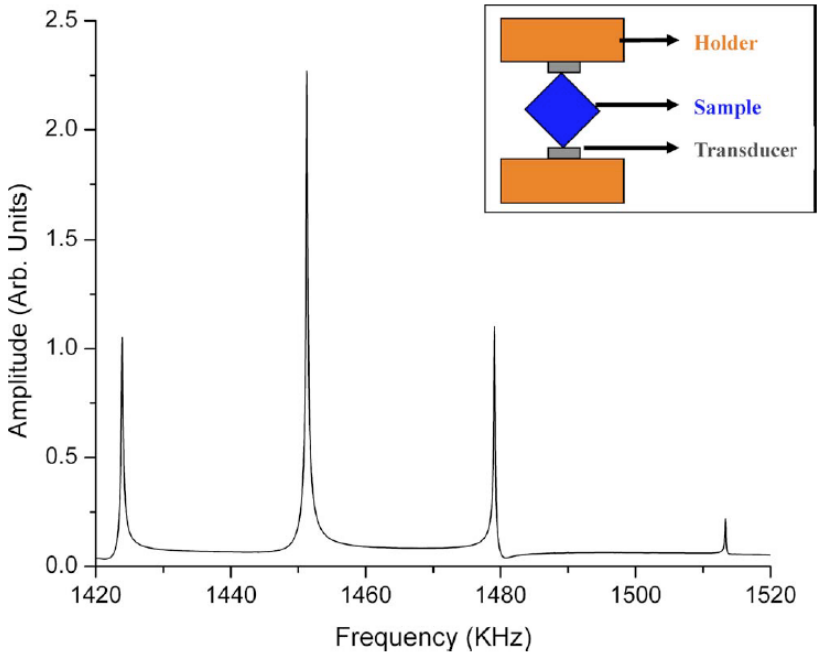

Figure 3.8: A typical resonance spectrum measured by RUS, after Luan *et al.* (2009)

3.8.2 Data collection and analysis

Figure 3.7 shows our home-built RUS probe which can be inserted in a Quantum Design PPMS or Versalab to determine elastic moduli as a function of temperature (2 - 380 K) and magnetic field (0 - 9 T). Crystals with cubic symmetry are aligned and cut into parallelepipeds with all faces perpendicular to the crystallographic $\langle 100 \rangle$ axes for RUS measurements. The sample is placed between two piezoelectric transducers, as shown in Figure 3.7 as well as the inset of Figure 3.8. A frequency generator creates an electromagnetic wave that is sent to the top transducer, which then converts the signal into a mechanical wave. The mechanical wave travels through the sample and the bottom transducer detects the mechanical signal and converts it back to an electrical signal. Thus, the mechanical resonances of a freely vibrating sample of known shape are measured, and a nonlinear optimization procedure is used to fit the full elastic tensor of the material Migliori *et al.* (1993). Figure 3.8 shows a typical resonance spectrum in the frequency range between 1420 kHz and 1520 kHz. These resonances are sharp as the mechanical dissipation is low ($Q = f/\Delta f \gg 1$, where f is the resonance frequency and Δf is the full width at half maximum). When Q is large, the dissipation is low, the resonance peak is sharp and the elastic moduli are well determined. Conversely, when Q is small, high ultrasonic absorption inhibits observance of enough resonance peaks, preventing determination of the full tensor. Nevertheless, the absolute values of different elastic constants scale with f^2 ($C_{ij} \sim f^2$), which usually allows for determination of elastic moduli in a broader temperature range.

Table 3.1 shows the RUS fit for a $EuTiO_3$ single crystal at 300 K. The complete elastic tensor (C_{11}, C_{12} and C_{44}) is extracted by fitting 25 resonance modes. The last three columns indicate the dependence of each line on C_{11}, C_{12} and C_{44} respectively. For example, the first resonance is 98 % C_{44} dependent, which allows for a determination of C_{44} through tracking the first resonance. Note that the rms

Table 3.1: Measured and fitted resonance frequencies of a $EuTiO_3$ single crystal at 300 K. The last three columns describe the fractional dependence of each mode frequency on each elastic modulus.

Modes	f measured	f fitted	%error	C11	C12	C44
1	1.163936	1.159448	-0.39	0.02	-0.01	0.98
2	1.459111	1.457061	-0.14	1.16	-0.34	0.18
3	1.477347	1.479414	0.14	1.15	-0.33	0.19
4	1.540103	1.534839	-0.34	0.06	-0.02	0.96
5	1.743892	1.751069	0.41	0.12	-0.03	0.91
6	1.773843	1.77777	0.22	1.49	-0.49	0
7	1.789575	1.788613	-0.05	0.14	-0.04	0.9
8	1.900502	1.901476	0.05	1.28	-0.42	0.14
9	1.921073	1.923345	0.12	0.54	-0.17	0.63
10	1.960585	1.958905	-0.09	1.5	-0.5	0.01
11	1.971882	1.968283	-0.18	0.94	-0.19	0.25
12	2.016699	2.023857	0.35	0.3	-0.05	0.75
13	2.08261	2.083562	0.05	0.95	-0.2	0.25
14	2.095701	2.097296	0.08	1.52	-0.52	0
15	2.168329	2.16662	-0.08	0.93	-0.25	0.32
16	2.235109	2.245543	0.47	0.89	-0.15	0.26
17	2.245284	2.245606	0.01	1	-0.27	0.27
18	2.286457	2.275601	-0.47	0.16	-0.05	0.9
19	2.317239	2.312527	-0.2	1.18	-0.23	0.05
20	2.436999	2.429924	-0.29	1.28	-0.29	0.01
21	2.502829	2.504385	0.06	1.25	-0.41	0.16
22	2.527385	2.520129	-0.29	0.97	-0.29	0.31
23	2.534996	2.532897	-0.08	1.02	-0.31	0.29
24	2.558189	2.567394	0.36	0.12	-0.01	0.89
25	2.671467	2.678652	0.27	0.49	-0.16	0.67
rms fit error	0.25%					
C11	309.4 Gpa					
C12	105.8 Gpa					
C44	116.9 Gpa					
bulk mudulus	173.6 Gpa					

fit error is 0.25 %, this is determined by a nonlinear least-squares minimizing the function defined by the sum of the weighted residuals

$$F = \sum_{i=1}^{N} w_i (f_i - g_i)^2 \tag{3.18}$$

where g_i and f_i are the vectors of the measured and calculated frequencies, and w_i is a weighting factor. Empirically, fitting errors below 0.6 % give trust-able elastic moduli values.

3.8.3 Applications to the study of structural phase transitions (SPT)

RUS can be applied to the fields of physics, materials science and earth science as the most sensitive probe for detecting structural, magnetic, and superconducting phase transitions Rehwald (1973). Here, we focus our discussion on structural phase transitions. The elastic behavior of a material without any thermodynamic "anomalies" can be modeled using the so-called Varshni function Varshni (1970)

$$C_{ij}(T) = C_{ij}^0 - \frac{s}{e^{t/T} - 1} \tag{3.19}$$

which predicts a gradual stiffening with decreasing temperature that levels off at low temperatures, as shown in Figure 3.9.

The behavior of elastic moduli upon phase transitions deviate from the Varshni function due to the coupling between strain (e) and order parameter (Q). There exist mainly three categories of couplings, and the corresponding elastic moduli behavior is shown in Figure 3.10.

1. Case (a) Coupling linear in the order parameter but quadratic in the strain $F_c = \delta Q e^2$ and a continuous transition. The elastic modulus is expected to soften to zero at T_C and rise up sharply afterwards.

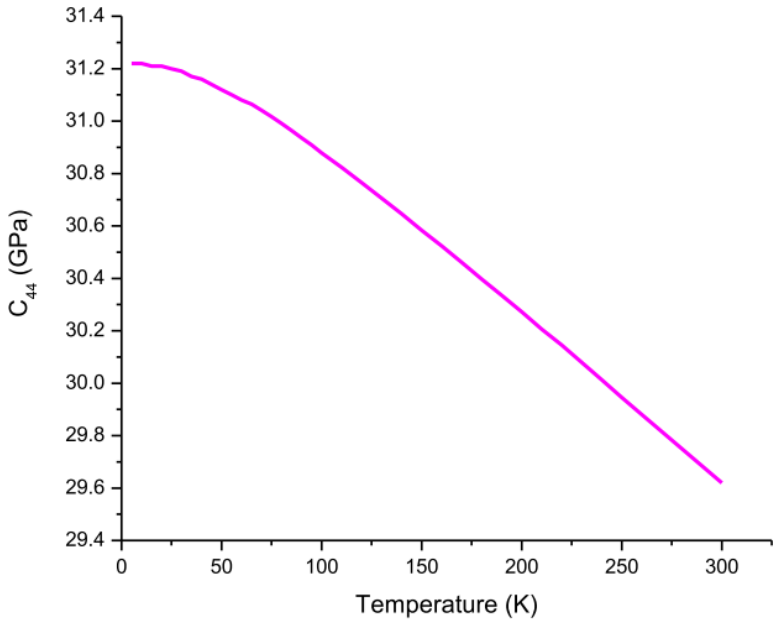

Figure 3.9: Typical elastic behavior of a system with no thermodynamic irregularities, after .

2. Case (b) Coupling linear in the strain and quadratic in the order parameter, $F_c = \gamma Q^2 e$ and a continuous transition. A step-like softening is expected upon the transition.

3. Case (c) Strain and order parameter are coupled linearly, $F_c = \beta Q e$ and a continuous transition. The elastic modulus is expected to remain flat and rise up when T approaches T_C.

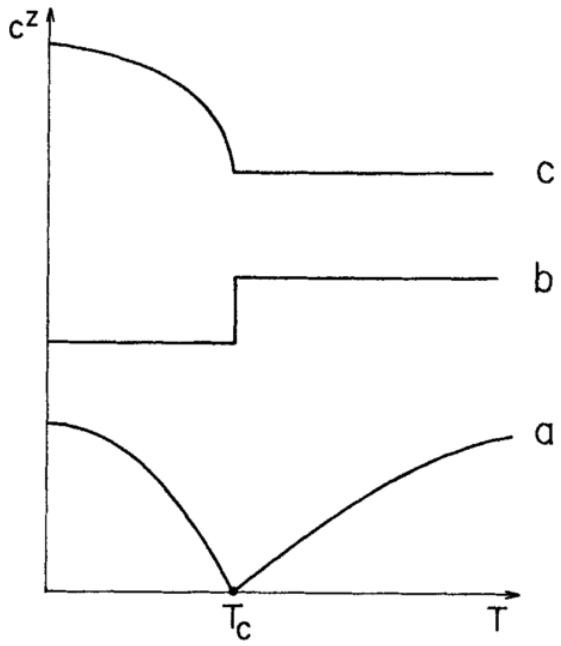

Figure 3.10: General behaviour of the elestic modulus C_{ij} at a continuous phase transition. The cases a, b and c are discussed in the text, after Rehwald (1973)

Chapter 4

Magnetic Phase Diagram of $\mathbf{EuTi_{1-x}}B_x\mathbf{O_3}$ (B = Zr, Nb)

In this chapter, we report the X-ray diffraction, *dc* magnetic susceptibility, heat capacity, and electrical resistivity data collected on polycrystalline $EuTi_{1-x}B_xO_3$ (B = Zr, Nb). A similar version of this chapter is published as L. Li, H. D. Zhou, J.-Q. Yan, D. Mandrus and V. Keppens, APL MATERIALS **2**, 110701 (2014).

4.1 Introduction

As mentioned in Chapter 1, divalent europium perovskite $EuTiO_3$ (ETO) has attracted considerable attention due to its large magnetoelectric effect, which manifests itself in a significant decrease of the dielectric constant at the G-type antiferromagnetic ordering temperature of 5.6 K Katsufuji & Takagi (2001). This coupling between spin and charge ordering indicates that ETO is a promising multiferroic material which could be widely used in the field of spintronics. The pioneering work on strained ETO thin films further confirms the multiferroic potential of this compound near room temperature and reveal an intricate balance between antiferromagnetic (AFM) and ferromagnetic (FM) interactions Lee *et al.* (2010). As

the dielectric, transport and magnetic properties of perovskite titanates $ATiO_3$ are easily tuned by perturbations like strain, pressure, or chemical doping, the possibility of strain induced ferromagnetism or ferroelectricity in bulk ETO can be explored through a study of chemical doping effects on the electrical and magnetic properties of this compound. The solid-solution systems $EuTiO_3$ - $EuZrO_3$ ($EuTi_{1-x}Zr_xO_3$) and $EuTiO_3$ - $EuNbO_3$ ($EuTi_{1-x}Nb_xO_3$) are particularly interesting as they allow evaluation of the effects of chemical pressure and charge carriers on the magnetic and transport properties of ETO. $EuZrO_3$ crystallizes in an orthorhombic structure and is an insulator with a G-type AFM ground state below a $T_N \approx 4.1$ K Viallet *et al.* (2008); Zong *et al.* (2010). It also presents a magnetoelectric effect which resembles that of ETO Kolodiazhnyi *et al.* (2010). In contrast, $EuNbO_3$ is a FM metal with a $T_C \approx 4$ K and $Pm\bar{3}m$ cubic crystal structure at all temperatures Zubkov *et al.* (1995a). Studies of $EuTi_{1-x}Zr_xO_3$ are limited to $x = 0.05$ Akahoshi *et al.* (2013) and there are only two studies on $EuTi_{1-x}Nb_xO_3$, reporting a significant increase in electrical conductivity in Nb-doped bulk samples Ishikawa *et al.* (1983) and the observation of ferromagnetism in Nb-doped thin films Kususe *et al.* (2014). In this chapter, results from magnetization, powder X-ray diffraction (XRD), heat capacity, and resistivity measurements on $EuTi_{1-x}B_xO_3$ (B = Zr, Nb) are reported. The data, collected on polycrystalline samples, allow us to address the influence of the crystal and electronic structures on the antiferromagnetic ordering in the parent compound.

4.2 Experimental details

Polycrystalline $EuTi_{1-x}Zr_xO_3$ ($x = 0, 0.015, 0.03, 0.05, 0.1, 0.15, 1$) and $EuTi_{1-x}Nb_xO_3$ ($x = 0, 0.015, 0.03, 0.05, 0.1, 0.2, 0.3, 0.4, 0.5$) samples were prepared as described in section 3.1.1. The powder samples were cold pressed Zhou *et al.* (2003) into dense pellets and subjected to further characterization. Powder X-ray diffraction patterns were recorded with a HUBER Imaging Plate Guinier Camera 670 with Ge monochromatized $CuK_{\alpha 1}$ radiation ($\lambda = 1.54059\mathring{A}$). Rietveld refinements were obtained using

FullProf Rodrguez-Carvajal (1993). The *dc* magnetic susceptibility measurements were carried out using a Quantum Design Magnetic Property Measurement System (MPMS) SQUID VSM in the temperature interval 2 K-300 K after cooling in either zero field (ZFC) or in a measuring field (FC) of 50 Oe. Hysteresis loops of magnetization M versus applied field H were obtained at 2 K over the range 5 T to 5 T. The specific heat measurements were performed in a Quantum Design Physical Property Measurement System (PPMS) between 2.5 K and 300 K. Electrical resistivity measurements were performed on dense cold-pressed samples by means of a four-probe method in a PPMS between 3 K and 300 K. Gold wires and silver epoxy were used to make contacts.

4.3 Results

XRD measurements at room temperature confirm that all samples are single phase and the diffraction patterns for $EuTi_{1-x}Zr_xO_3$ ($x = 0, 0.015, 0.03, 0.05$) and $EuTi_{1-x}Nb_xO_3$ (x between 0 and 0.5) were successfully refined using the cubic $Pm\bar{3}m$ space group. $EuTi_{1-x}Zr_xO_3$ samples with higher doping concentrations show deviations from cubic symmetry. Figure 4.1 shows that the lattice parameter of the cubic systems follows Vegards law and increases linearly with increasing doping x, indicating a good solid solution.

Figure 4.2 shows the temperature dependence of the magnetic susceptibility $\chi = M/H$ for $EuTi_{1-x}Zr_xO_3$ over the temperature range 2 K $\leq$ T $\leq$ 20 K. There is no noticeable distinction between ZFC and FC data, and all of the samples exhibit an AFM transition below T_N which manifests itself as a sharp cusp. As shown in the inset of Figure 4.2(a), the M vs. H curves at 2 K for $EuTi_{1-x}Zr_xO_3$ ($x = 0, 0.05, 0.1$) exhibit a linear increase with increasing H and saturate at H values of about 1.5 T with a moment of approximately 7.5 μ_B/Eu^{2+}. It is clear from χ vs. T (Figure 4.2(a)) that Zr doping decreases T_N to lower temperatures, which is also observed in specific heat measurements (Figure 4.2(b)). Distinct λ anomalies corresponding to the AFM

transitions are observed in the temperature dependence of molar heat capacity. The Neel temperature T_N is marked with an arrow in Figure 4.2(b).

Figure 4.3(a) shows the temperature dependence of M/H for $EuTi_{1-x}Nb_xO_3$ between 2 K and 30 K. The undoped $EuTiO_3$ and lightly doped ($x \leq 0.05$) samples show a cusp at T_N. However, the M/H vs. T curves show a strong increase when x exceeds 0.05 which denotes the onset of a magnetic transition from paramagnetic to ferromagnetic. A fit of M/H vs. T data measured at 1000 Oe to the Curie-Weiss law $\chi(T) = C/(T - \theta)$ in the range 100-300 K yields an effective moment ranging from 7.92 to 8.88 μ_B, which is close to the calculated effective moment

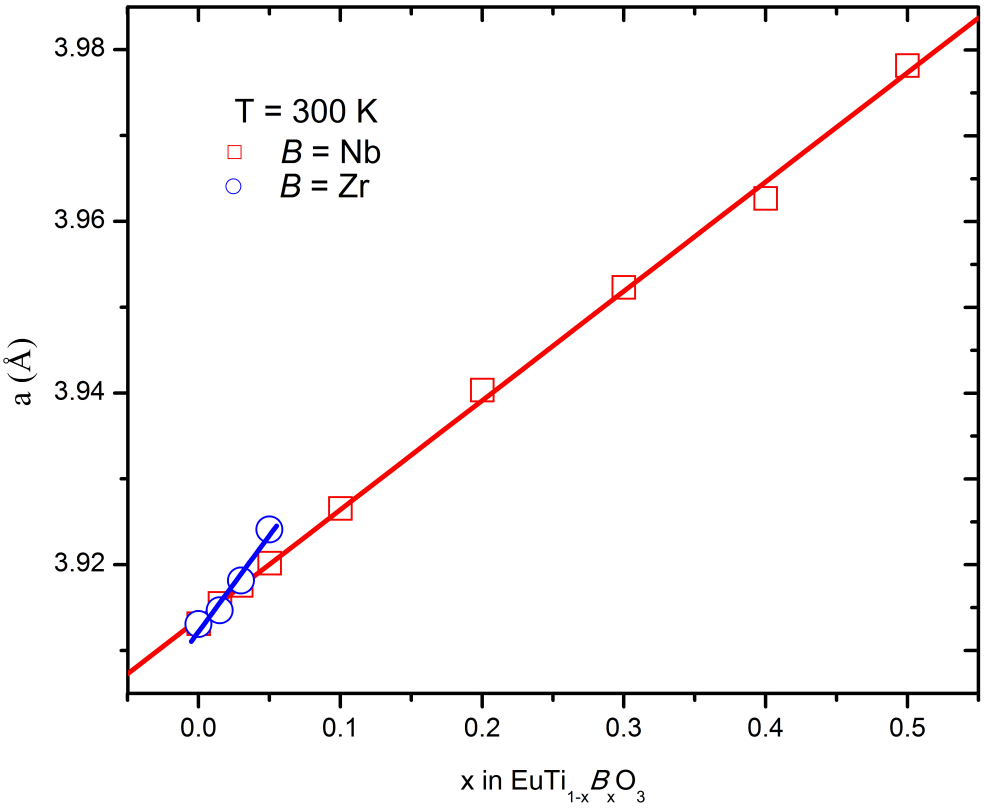

Figure 4.1: Variation of the lattice parameters with doping concentration x for $EuTi_{1-x}B_xO_3$ (B = Nb, Zr).

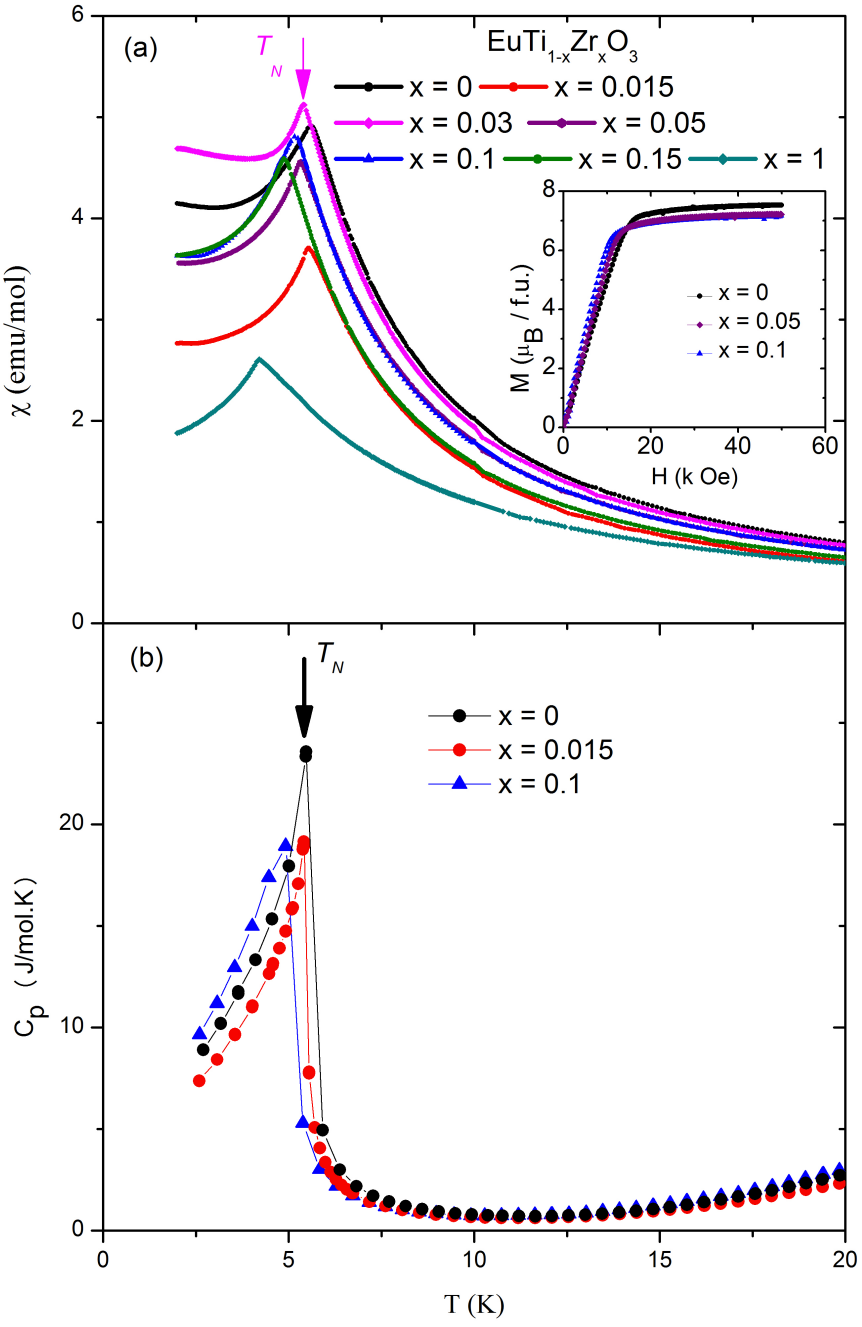

Figure 4.2: Temperature dependence of (a) ZFC susceptibility under 50 Oe and (b) molar heat capacity for $EuTi_{1-x}Zr_xO_3$ ($0 \leq x \leq 1$). The inset of (a) shows the M vs. H curves at 2 K.

of free Eu^{2+} (7.93 μ_B). The inset of Figure 4.3(a) shows the field dependence of magnetization at 2 K in the range 0 T - 5 T for $EuTiO_3$ and $EuTi_{0.8}Nb_{0.2}O_3$. No apparent hysteresis loop is observed for FM $EuTi_{0.8}Nb_{0.2}O_3$. This behavior is not unusual for Eu ferromagnets as they are typically soft ferromagnets with very small coercive fields Sales *et al.* (2001). Nb-doped $EuTiO_3$ has a slightly higher saturation moment than the parent compound. In Figure 4.3(b), we plot the molar heat capacity *vs.* temperature for $EuTi_{1-x}Nb_xO_3$. The λ anomalies are associated with a transition to antiferromagnetism for $x \leq 0.05$ samples and ferromagnetism for $x \geq 0.2$ samples. For $0.1 \leq x \leq 0.16$, two transitions are present below 10 K, which manifest themselves in both susceptibility and heat capacity measurements. This phenomenon is possibly associated with either a chemical inhomogeneity or the coexistence of two magnetic phases.

Figure 4.4 shows the temperature dependence of the electrical resistivity for $EuTi_{1-x}Nb_xO_3$ (x = 0.015, 0.2, and 0.4) and $EuTi_{0.97}Zr_{0.03}O_3$. Pure $EuTiO_3$ is reported to be a band insulator. The inset of Figure 4.4 shows that $EuTi_{0.97}Zr_{0.03}O_3$ is still highly insulating while the resistivity of $EuTi_{0.985}Nb_{0.015}O_3$ is significantly reduced. Increased Nb doping results in metallic behavior, as shown in Figure 4.4 for $x = 0.2$ and 0.4 samples. The cusps at low temperatures are associated with the FM transitions.

The valence of the Nb-dopant can in principle be either 4+ or 5+. As the $EuTi_{1-x}Nb_xO_3$ samples were synthesized in a reducing atmosphere, using NbO_2 as a starting material, it is most likely that the valence remains 4+. This is supported by the observation that the Curie temperature for $EuTi_{1-x}Nb_xO_3$ is similar to the Curie temperature for $EuTiO_3$ doped with an equal percentage of La on the A-site Katsufuji & Tokura (1999), suggesting that the carrier concentration is the same. While we cannot completely rule out the possibility of 5+ valence, it is worth pointing out that with either a 4+ or a 5+ valence each Nb will donate one itinerant electron to the system. As the ionic radii of Nb^{4+} and Zr^{4+} are both larger than that of Ti^{4+}, both dopants apply a negative chemical pressure to the system. The difference between

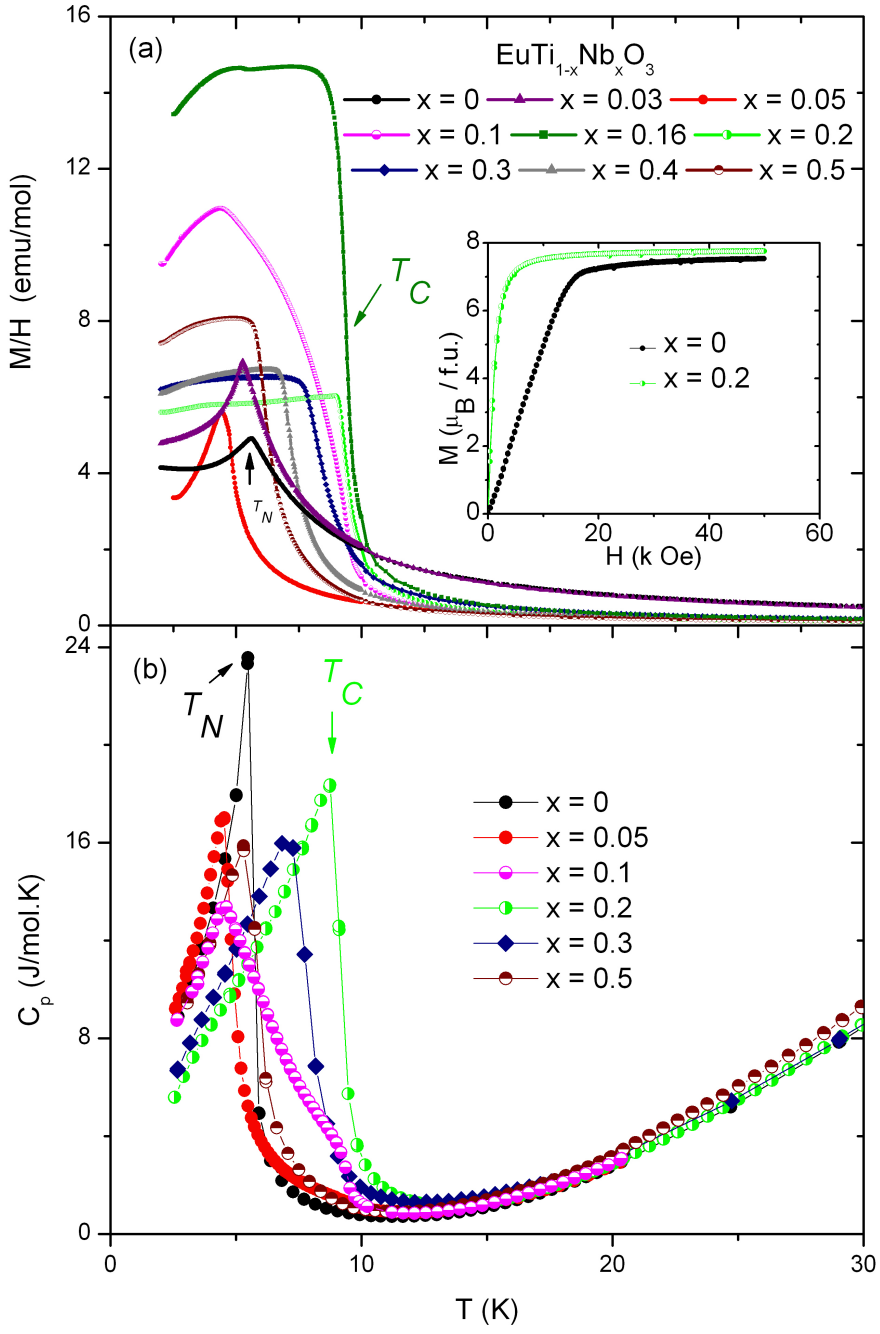

Figure 4.3: Temperature dependence of (a) ZFC susceptibility under 50 Oe and (b) molar heat capacity for $EuTi_{1-x}Nb_xO_3$ ($0 \leq x \leq 1$). The inset of (a) shows the $Mvs.H$ curves at 2 K.

Nb doping and Zr doping is that Nb^{4+} has one unpaired electron in its $4d$ shell while Zr^{4+} does not have any d electrons. Ti^{4+} has an empty $3d$ shell. A study of Zr- and Nb-doped ETO therefore allows us to compare the effects of pure chemical pressure and an extra d electron on the Ti site on the magnetic properties of this system. In view of the delicate balance between AFM and FM ground states in the band insulator ETO Akamatsu *et al.* (2011), it is extremely intriguing to look into the effects of electronic and crystal structures on the magnetic ground state of ETO.

In Figure 4.5, we present the low-temperature magnetic phase diagram of $EuTi_{1-x}B_xO_3$ (B = Zr, Nb). All of the $EuTi_{1-x}Zr_xO_3$ compounds exhibit AFM

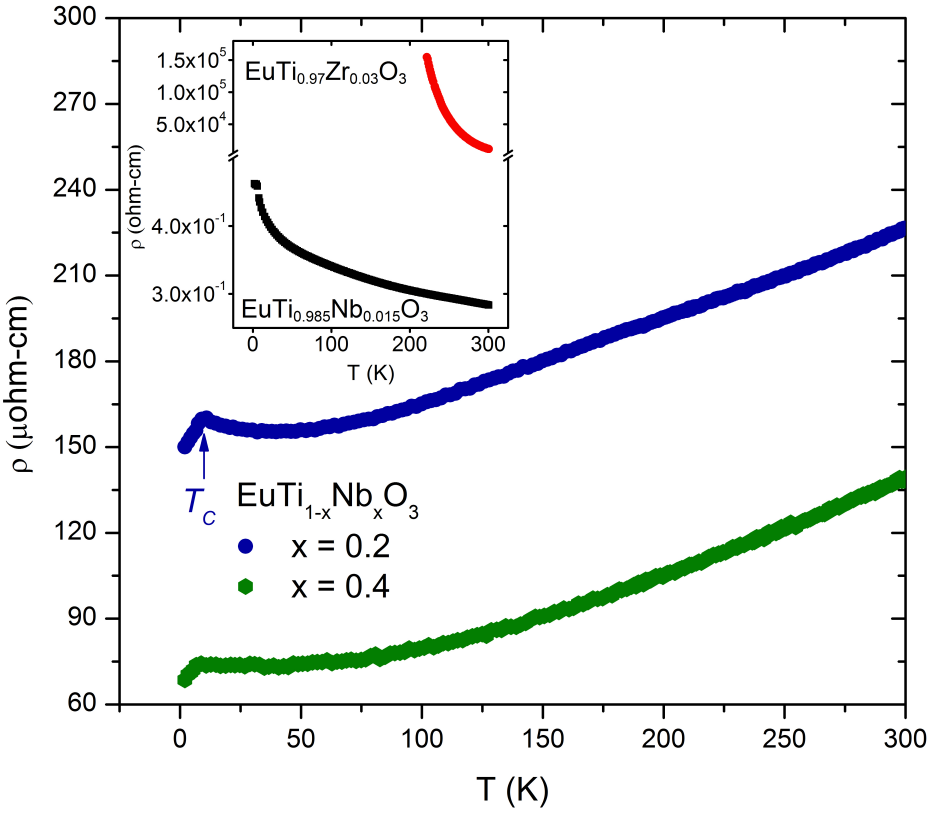

Figure 4.4: Resistivity *vs.* T for $EuTi_{1-x}Nb_xO_3$ (x = 0.015, 0.2, and 0.4) and $EuTi_{0.97}Zr_{0.03}O_3$.

ground states with T_N decreasing nonlinearly with increasing Zr doping x from 5.6 K ($EuTiO_3$) to 4.1 K ($EuZrO_3$). It has been suggested from first principle calculations that the strength of AFM interaction in $EuMO_3$ (M = Ti, Zr, Hf) is closely related to both crystal and electronic structures Akamatsu *et al.* (2013). Substitution of Ti by Zr increases the band gap between Eu $4f$ and M nd states, which weakens the Eu $4f$ superexchange interactions via the M nd states Akamatsu *et al.* (2013), evidenced by a decrease in the Neel temperature.

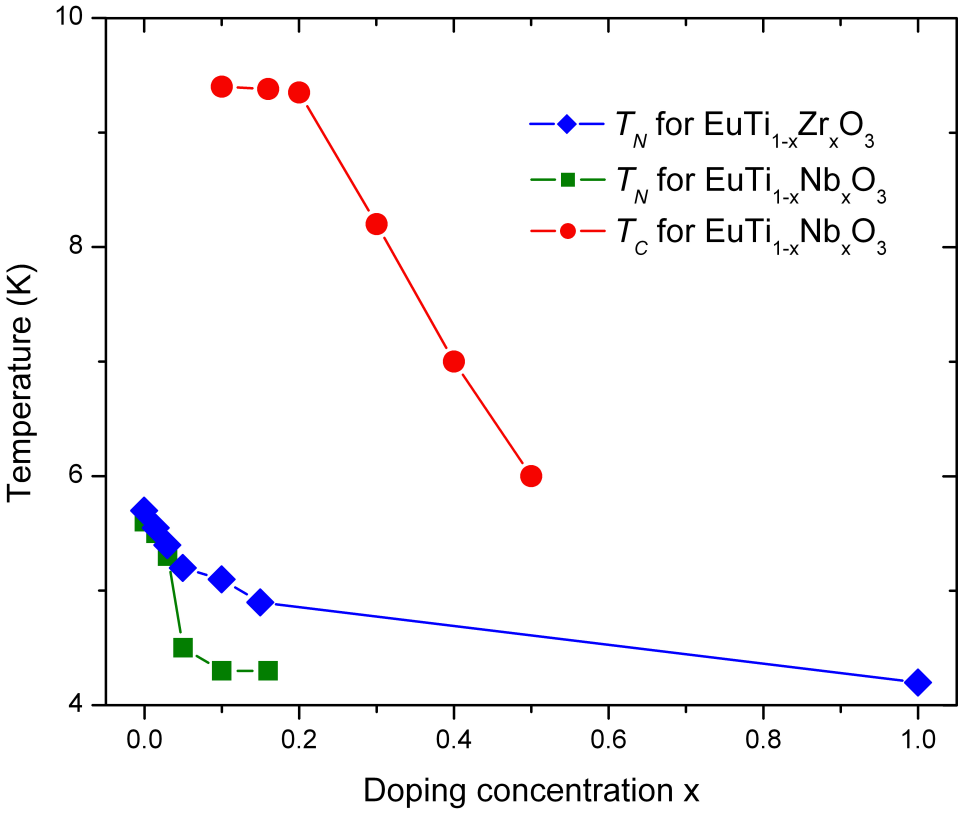

Figure 4.5: The magnetic phase diagram of $EuTi_{1-x}Zr_xO_3$ and $EuTi_{1-x}Nb_xO_3$ as determined from magnetic susceptibility measurements. T_C is defined as the maximum point in the plot of dM vs. T. It should be noted that for Nb doping concentration x between 0.1 and 0.16, mixed AFM and FM phases coexist.

4.4 Discussion

Guguchia et al. Guguchia *et al.* (2013) have investigated the physical pressure effect on the magnetic properties of a polycrystalline ETO sample and found that pressure raises T_N to higher temperatures and no ferromagnetism was achieved. The robust antiferromagnetism in $EuTi_{1-x}Zr_xO_3$ further rules out the possibility of pure chemical pressure as the factor to induce ferromagnetism. On the other hand, ferromagnetism has been observed in oxygen deficient $EuTiO_3$ thin films Kugimiya *et al.* (2007), Nb-doped ETO thin films Kususe *et al.* (2014), and strained ETO thin films Lee *et al.* (2010). In addition, lanthanum-doped ETO is converted to FM Katsufuji & Tokura (1999); Yoshii *et al.* (2003). The electrical resistivity in the La-doped compounds is significantly reduced suggesting itinerant electrons, and the induced ferromagnetism was explained in terms of a RudermanKittelKasuyaYosida (RKKY)- type magnetic interaction between the localized Eu moments via itinerant $3d$ electrons Katsufuji & Tokura (1999); Yoshii *et al.* (2003). Substituting Nb^{4+} ($4d^1$) for Ti^{4+} ($3d^0$) is an alternative way to introduce an electron into a B site, allowing us to explore the effect of doping on multiferroicity. Previous work Ishikawa *et al.* (1983) along with our resistivity data indicates that Nb doping increases the electrical conductivity dramatically, suggesting that Nb doping pushes the system towards the itinerant limit. Our magnetization measurements on $EuTi_{1-x}Nb_xO_3$ have indicated that FM behavior starts to set in when x exceeds 0.05 and exclusively takes over the magnetic ground state when $x \geq 0.2$. Furthermore, our isothermal magnetization measurements at 2 K show that these ferromagnets require a very small field (≈ 0.5 T) to saturate the magnetization, possibly due to the lack of spin-orbit coupling ($L = 0$ for Eu^{+2}). As seen in Figure 4.5, the Curie temperature T_C reaches a maximum of 9.4 K at $x \approx 0.1$ and decreases with further doping, which is very similar to $Eu_{1-x}R_xTiO_3$ (R = La and Gd) Katsufuji & Tokura (1999).

4.5 Conclusion

In this chapter, we report the magnetic and transport properties of $EuTi_{1-x}B_xO_3$ (B = Zr, Nb). The magnetic phase diagram was constructed by measuring magnetization and heat capacity. Zr doping reduces the $f-d$ hybridization, and, as a consequence, all of the $EuTi_{1-x}Zr_xO_3$ compounds exhibit AFM ordering below T_N, where T_N decreases nonlinearly from 5.6 K ($EuTiO_3$) to 4.1 K ($EuZrO_3$) with increasing Zr doping x. Whereas a similar decrease in T_N is observed for small amounts of Nb doping ($x \leqslant 0.05$), ferromagnetism is induced in $EuTi_{1-x}Nb_xO_3$ with $x \geq 0.05$. The Curie temperature T_C reaches a maximum of 9.4 K at $x \approx 0.1$ and decreases with further Nb doping. While Zr-doped compounds remain insulating, Nb-doped ones become metallic. We propose that the FM interaction between localized Eu f spins mediated by itinerant electrons results in the induced ferromagnetism in $EuTi_{1-x}Nb_xO_3$. Our study highlights the importance of Eu $4f$-B nd-Eu $4f$ interaction in determining the magnetic ground state of $EuTiO_3$.

Chapter 5

Structural and Magnetic Phase Transitions in $EuTi_{1-x}Nb_xO_3$

In this chapter, we investigate the structural and magnetic phase transitions in $EuTi_{1-x}Nb_xO_3$ ($0 \leq x \leq 0.3$) with synchrotron powder X-ray diffraction (XRD), resonant ultrasound spectroscopy (RUS), and magnetization measurements. Upon Nb-doping, the $Pm\bar{3}m \leftrightarrow I4/mcm$ structural transition shifts to higher temperatures and the room temperature lattice parameter increases while the magnitude of the octahedral tilting decreases. In addition, Nb substitution for Ti destabilizes the antiferromagnetic ground state of the parent compound and long range ferromagnetic order is observed in the samples with $x \geq 0.1$. The structural transition in pure and doped compounds is marked by a step-like softening of the elastic moduli in a narrow temperature interval near T_S, which resembles that of $SrTiO_3$ and can be adequately modeled using the Landau free energy model employing the same coupling between strain and octahedral tilting order parameter as previously used to model $SrTiO_3$. Most of the content in this chapter is published in L. Li, J. R.Morris, M. Koehler, Z.L.D, H. D. Zhou, J.-Q. Yan, D. Mandrus and V. Keppens, accepted, Phys. Rev. B (2015)."

5.1 Introduction

The tilting of the oxygen octahedra in cubic perovskites is known to induce structural phase transitions, which are often associated with the emergence of intriguing physical phenomena Imada *et al.* (1998). $SrTiO_3$ (STO) is one of the most extensively studied perovskite oxides for its structural phase transition (SPT) at $T_S \approx 105$ K Fleury *et al.* (1968); Shirane & Yamada (1969). This SPT has been recognized as the paradigm of a displacive transition, nevertheless, proven to carry some order/disorder element Bruce *et al.* (1979); Bussmann-Holder *et al.* (2007). In the past decade, the discovery of the magnetoelectric coupling in iso-structural $EuTiO_3$ (ETO) has generated substantial interest in this compound Katsufuji & Takagi (2001). This coupling manifests itself in a significant decrease of the dielectric constant at the G-type antiferromagnetic ordering temperature $T_N \approx 5.6$ K Katsufuji & Takagi (2001). In analogy to STO, ETO also undergoes an antiferrodistortive SPT from $Pm\bar{3}m$ to $I4/mcm$ ($a^0a^0c^-$ in Glazer notation) driven by R-point phonon softening Ellis *et al.* (2012). While the SPT at 105 K in STO has been extensively studied for decades, the transition in ETO was observed only recently Bussmann-Holder *et al.* (2011) but has since attracted much attention in the field and has been the focus of numerous experimental Taylor *et al.* (2012); Allieta *et al.* (2012); Goian *et al.* (2012); Guguchia *et al.* (2012); Ellis *et al.* (2012); Kim *et al.* (2013); Ellis *et al.* (2014); Bessas *et al.* (2013) and theoretical Rushchanskii *et al.* (2012); Yang *et al.* (2012); Birol & Fennie (2013) studies.

Previous synchrotron powder X-ray diffraction (XRD) indicates a $T_S \approx 235$ K for ETO Allieta *et al.* (2012), which is significantly lower than $T_A \approx 282$ K suggested by heat capacity measurement Bussmann-Holder *et al.* (2011). This discrepancy draws attention to the possible local tetragonal distortions present above 235 K, as evidenced by pair distribution function analysis Allieta *et al.* (2012). Kim *et al.* Kim *et al.* (2013) identified incommensurate satellite peaks below 285 K in single crystal synchrotron XRD, and proposed a dynamically modulated equilibrium state between 285 K and 160 K, incorporating antiferrodistortive instabilities of TiO_6 octahedra

accompanied by antiferroelectric displacements of Ti atoms. Conversely, a simple and un-modulated structure is claimed for ETO, as evidenced by the commensurate superlattice peaks at $T = 250$ K in single crystal XRD Ellis *et al.* (2014), and the R-point acoustic phonon softening that is similar to the soft modes in STO Ellis *et al.* (2012). ETO samples synthesized under different conditions were studied Goian *et al.* (2012). While one of the ceramic samples shows a simple cubic-to-tetragonal long range transformation near 300 K, the other ceramic samples as well as the single crystal present an incommensurate structure at low temperature. These discrepancies were considered to arise from variations in sample preparation conditions, which lead to mixed valence on the Eu-site and/or oxygen non-stoichiometry and therefore could potentially alter the physical properties. This was further confirmed by Kennedy et al. Kennedy *et al.* (2014), who show that the electrical resistivity of $EuTiO_{3-\delta}$ is significantly reduced with oxygen vacancies due to the change of Ti^{4+} to Ti^{3+} when oxygen vacancies and/or trivalent Eu are present. Very recently, the elastic response near 1 MHz of an irregularly shaped ETO single crystal was examined using resonant ultrasound spectroscopy (RUS) Spalek *et al.* (2014). A pronounced step-like shear softening near $T_S \approx 284$ K confirms that the SPT in STO and ETO is very similar in nature but takes place at very different temperatures.

Despite the recent studies of the nature and T_S of the SPT in ETO, the dramatic difference in T_S between STO and ETO is not well understood (the Goldschmidt tolerance factor t predicts a similar T_S for these two compounds) and may signal the importance of the spin-phonon coupling in ETO Lee *et al.* (2010). First-principles calculations suggested that the hybridization between Eu-f and Ti-d orbitals enhances the tilting of the octahedra and therefore T_S Birol & Fennie (2013). To examine how the T_S of the ETO system is influenced by the hybridization between Eu-f, (Ti, Nb)-d, and O-p orbitals, we have initiated the study of $EuTi_{1-x}Nb_xO_3$. Nb doping introduces itinerant electrons into this system, which mediate the magnetic interactions between Eu $4f$ spins and result in ferromagnetism Li *et al.* (2014). In the present paper, we extend the RUS study by Spalek *et al.* Spalek *et al.* (2014) and report the full elastic

tensor of single crystals of ETO as well as mixed crystals of $EuTi_{1-x}Nb_xO_3$. The dramatic change in the elastic constants allows for an accurate determination of T_S, and the potential impact of the orbital hybridization on T_S can be addressed. The amplitude of octahedral rotations at 100 K is determined from synchrotron X-ray powder diffraction data, and the role of Nb doping on the structural and magnetic instabilities will be discussed.

5.2 Methods

$EuTi_{1-x}Nb_xO_3$ polycrystals ($0 \leq x \leq 0.3$) along with single crystals (x = 0, 0.05, 0.1 and 0.2), and $EuTi_{1-x}Zr_xO_3$ single crystals (x = 0, 0.005, and 0.015) have been synthesized using floating zone technique as described in Chapter 3. Good crystal quality was confirmed by clear, round spots in the Laue back scattering pattern, and the single crystals were oriented with $Pm\bar{3}m$ symmetry and cut to rectangular parallelepipeds with all faces perpendicular to the crystallographic $\langle 100 \rangle$ axes for RUS measurement. The edge dimensions of the $EuTi_{1-x}B_xO_3$ (B = Nb, Zr) crystals for RUS measurements range between 0.5 mm and 2.5 mm. Since the Eu^{3+} impurities may influence the T_S Goian *et al.* (2012); Sagarna *et al.* (2014); Zhandun *et al.* (2015), our ETO crystal was carefully characterized before performing RUS measurements.

Room and low temperature X-ray diffraction (XRD) was first performed with a laboratory HUBER Imaging Plate Guinier Camera 670 with Ge monochromatized $CuK_{\alpha 1}$ radiation ($\lambda = 1.54059\mathring{A}$), confirming all samples to be single phase. To better resolve the tetragonal distortion, synchrotron powder XRD was performed through a mail-in program at the 11-BM beamline of the Advanced Photon Source at Argonne National Laboratory. Single crystals of $EuTi_{1-x}Nb_xO_3$ (x = 0, 0.05, 0.1 and 0.2) were ground to fine powders and loaded in a capillary tube with a diameter of 0.8 mm. The experiments were carried out with a fixed wavelength ($E = 30\ keV$, $\lambda = 0.41396(1)\mathring{A}$) at T = 295 K and 100 K. Rietveld refinements were obtained using the program GSAS Toby (2001). The magnetization measurements were performed

using a Quantum Design Magnetic Property Measurement System in the temperature interval 2 K to 300 K after cooling in either zero field (ZFC) or in a measuring field (FC) as described in Chapter 3. Thermogravimetric analysis (TGA) was employed to determine the oxygen content of ETO from the weight gain due to oxidation of Eu^{2+} to Eu^{3+}. The ETO crystals were found to be oxygen stoichiometric within experimental error.

5.3 Results

5.3.1 X-ray diffraction

Figure 5.1(a) and (b) show the Rietveld refinements from synchrotron XRD for the parent ETO at 295 K and 100 K, respectively. While the pattern at 295 K was refined with the $Pm\bar{3}m$ space group with lattice parameter $a = 3.9047(3)$ $\mathring{A}$, the pattern at 100 K was refined using $I4/mcm$ symmetry, yielding lattice parameters $a_{Tetra} = \sqrt{2}a_{Cub} = 5.51168(3)\mathring{A}$ and $c_{Tetra} = 2c_{Cub} = 7.81613(5)\mathring{A}$, in good agreement with previously reported values Allieta *et al.* (2012). Furthermore, the 295 K synchrotron XRD patterns of all samples show no well-defined peak splitting and could be adequately fitted with a cubic $Pm\bar{3}m$ model, whereas the 100 K patterns show well-resolved peak splitting and were fitted with a tetragonal $I4/mcm$ model. The room temperature lattice parameter extracted from Rietveld refinements obeys Vegard's law, and increases linearly with increasing x in $EuTi_{1-x}Nb_xO_3$. The symmetry lowering at 100 K was evidenced by the (200) peak splitting highlighted in the insets to Figure 5.1.

As shown in Figure 5.2, no readily apparent peak splitting due to the structural transition was observed at room temperature. However, we noticed significant peak broadening with increasing Nb content. This is demonstrated more clearly in Figure 5.3 in which we plotted the peak width of the (200) reflection at 295 K and splitting amplitude of (200) at 100 K obtained by a Lorentzian fit. Nb doping induces disorder

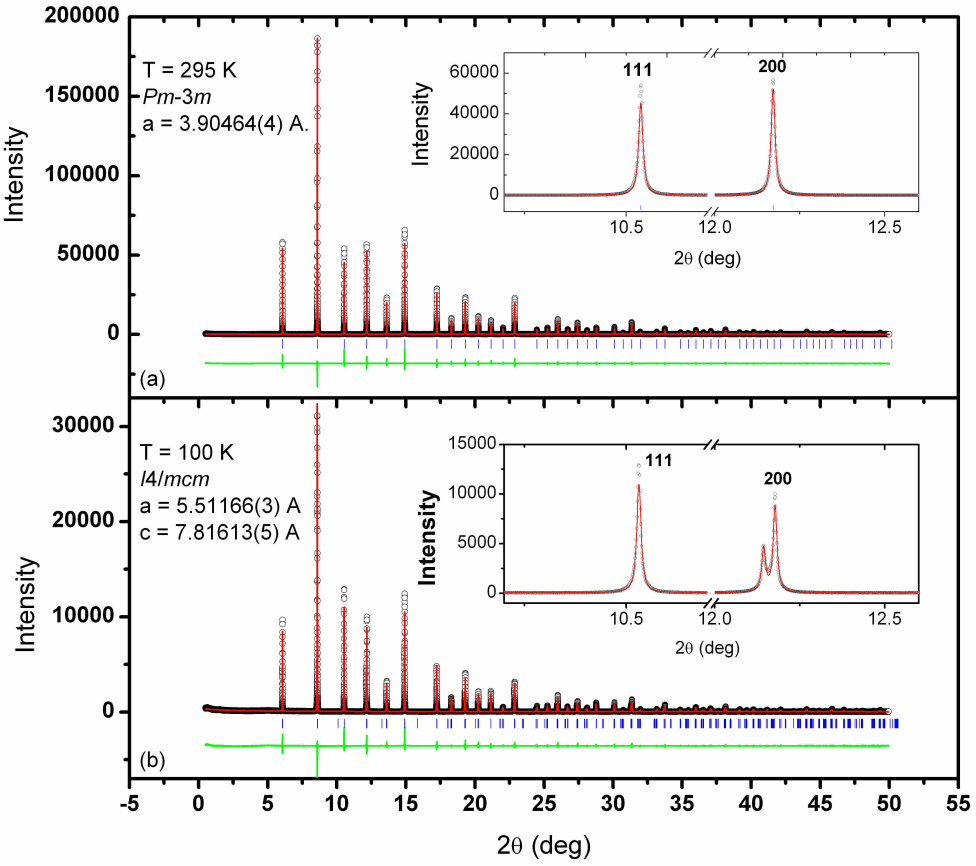

Figure 5.1: Rietveld refinements of the synchrotron X-ray powder patterns of $EuTiO_3$ collected at (a)295 K and (b)100 K respectively. The insets show the (111) and (200) reflections.

in the lattice, which can naturally explain the peak broadening. However, we believe that the peak splitting due to the structural transition also contributes to the peak broadening at 295 K since the SPT takes place above room temperature as revealed by RUS measurements. Intriguingly, the splitting amplitude at 100 K, which is proportional to the magnitude of the lattice distortion c/a ratio, is suppressed with increasing Nb doping, suggesting that Nb doping weakens the octahedral tilting in the ETO system.

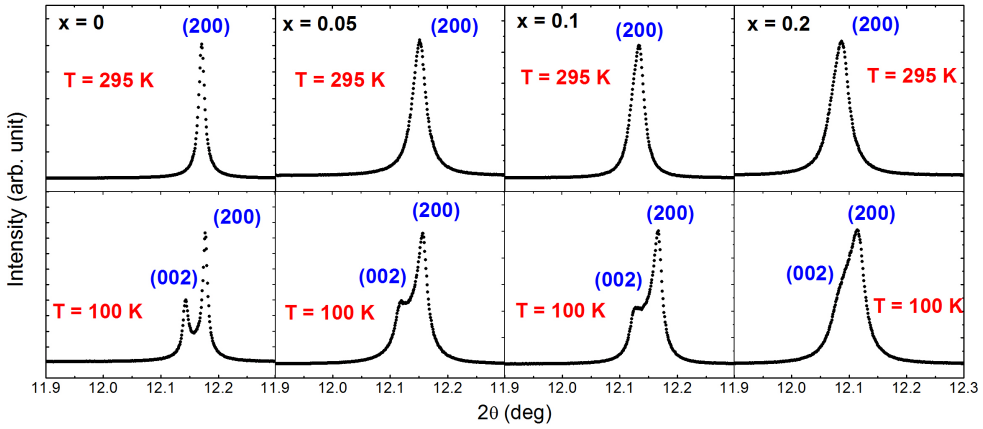

Figure 5.2: (200) peak splitting at 100 K for $EuTi_{1-x}Nb_xO_3$ (x = 0, 0.05, 0.1 and 0.2).

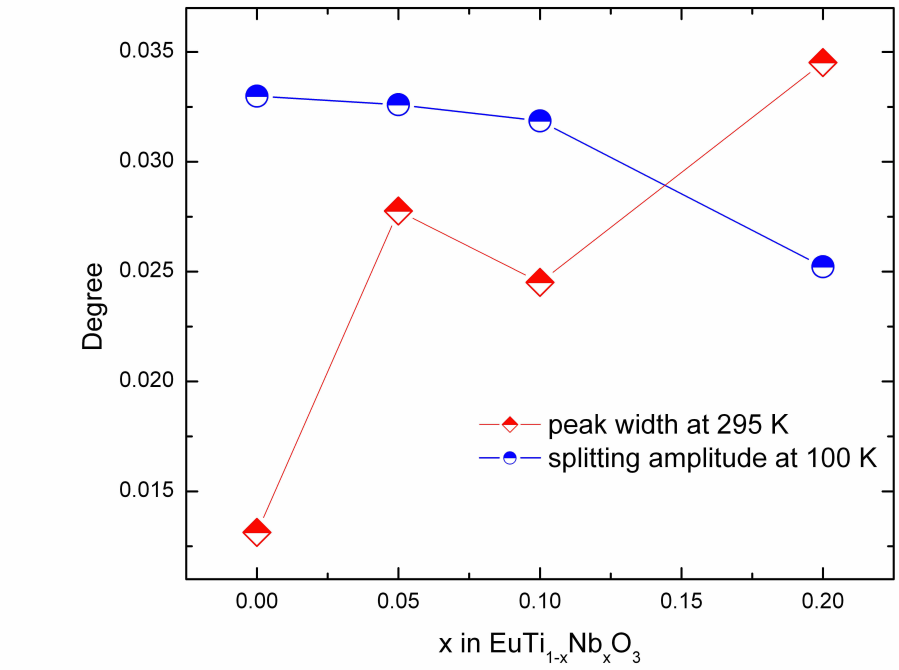

Figure 5.3: The (200) peak width at 295 K and splitting amplitude at 100 K for $EuTi_{1-x}Nb_xO_3$.

5.3.2 Magnetization

Figure 5.4 shows the temperature dependence of magnetization for $EuTi_{1-x}Nb_xO_3$ single crystals, plotted as (a) M/H under 50 Oe, and (b) H/M under 1000 Oe. The ZFC and FC curves of the parent ETO overlap, and reveal a $T_N \approx 5.7$ K. The data under 1000 Oe between 200 K and 300 K could be well fitted by the Curie-Weiss law, yielding a positive Weiss temperature of 3.48(1) K and an effective moment of approximately 8.35(1) μ_B, which agree well with literature values Katsufuji & Takagi (2001). A dramatic divergence between ZFC and FC curves is present for x = 0.05 sample, which may signal a spin glass behavior arising from the competition between AFM and FM interactions present in this system. The magnetic ground state of samples with $x \geq 0.1$ is switched from AFM to FM, as previously reported for polycrystalline samples Li *et al.* (2014). It is noteworthy that Nb doping induces metallic behavior Li *et al.* (2014). The induced ferromagnetism most likely results from the ferromagnetic interaction between localized Eu $4f$ spins, mediated by itinerant electrons introduced by chemical doping Katsufuji & Tokura (1999); Li *et al.* (2014).

Table 5.1: Effective moment and Weiss temperature for $EuTi_{1-x}Nb_xO_3$ single crystals derived from Curie - Weiss fits.

x	0	0.05	0.1	0.2
μ_{eff} (μ_B)	8.36	7.86	8.02	7.96
θ (K)	3.48	5.91	5.14	15.29

5.3.3 Elastic moduli

Cubic systems exhibit three independent elastic constants C_{11}, C_{12} and C_{44}. Note that C_{11} and C_{44} govern respectively longitudinal and transverse waves propagating along [100]. In the [110] direction, longitudinal waves are governed by $C_{L[110]} = \frac{1}{2}(C_{11} + C_{12} + 2C_{44})$, while one transverse wave is governed by C_{44}, the other by $C_{T[110]} = \frac{1}{2}(C_{11} - C_{12}) = C'$. In Fig. 5 we plot the temperature dependence of C_{44}. Below T_S,

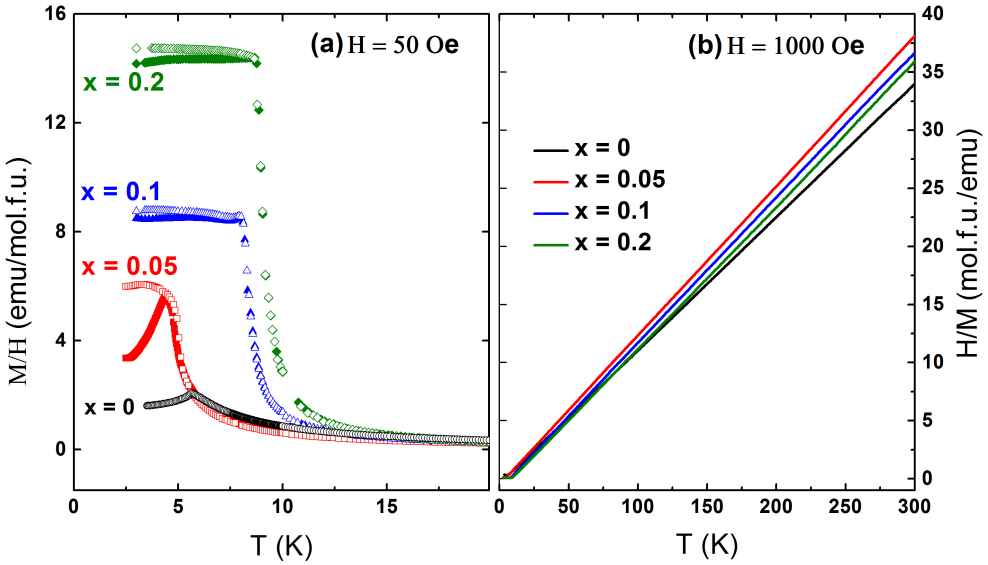

Figure 5.4: Temperature dependence of *dc* susceptibility for single crystals of $EuTi_{1-x}Nb_xO_3$ (x= 0, 0.05, 0.1, 0.2) in an applied field of 50 Oe. The full and empty symbols denote ZFC and FC data, respectively.

the ultrasonic absorption of the sample is so large that not enough resonances can be observed to allow an accurate determination of all three elastic moduli. However, the high temperature fit indicates that the lowest resonant frequency depends almost exclusively on C_{44}. This frequency is visible throughout the entire transition and below, allowing determination of the shear modulus over the entire temperature range. The striking feature in Fig. 5 is the step-like elastic softening of C_{44} at $T_S \approx 288$ K, which is reminiscent of the 105 K elastic anomaly observed in the elastic moduli of STO Bell & Rupprecht (1963a). The softening at T_S is accompanied by a dramatic rise in the internal friction Q^{-1} as a consequence of domain wall motion driven by elastic waves, which causes a significant broadening and deterioration of the resonances, preventing determination of the full tensor, as discussed above.

Table 5.2: T_S, density, and elastic moduli for single crystals of STO, ETO and ETO-Nb.

Sample	T_S (K)	Density (g/cm^3)	C_{11} (GPa)	C_{44} (GPa)	C' (GPa)	error%
STO(295 K)	105	5.015	311.58	120.83	107.2	0.3507
ETO(295 K)	288	6.744	307.24	116.3	100.06	0.2323
ETO(370 K)	288	6.744	3.0976	1.1695	102.57	0.2833
ETO-5%Nb(370 K)	322	6.809	3.1607	1.1256	104.365	0.1467
ETO-10%Nb(370 K)	353	6.758	3.0629	1.0923	100.315	0.3138

Figure 5.6 presents the temperature dependence of C_{11}, C_{44} and C' for single crystals of $EuTi_{1-x}Nb_xO_3$ (x = 0, 0.05 and 0.1) both in the absence of field and under applied magnetic fields up to 9 Tesla. The following features are noteworthy:

1) The substitution of Nb^{4+} for Ti^{4+} (up to x = 0.1) does not change the qualitative behavior of the elastic response near the SPT, and the step-like elastic softening as the temperature approaches T_S remains the most striking feature.

2) The transition temperature T_S is shifted to higher temperatures with increasing Nb doping, T_S = 288 K, 322 K and 353 K for x = 0, 0.05 and 0.1 respectively.

3) The elastic response of pure ETO does not show an observable magnetic field dependence in fields as high as 9 Tesla. However, if the 0 Tesla data is subtracted from the 9 Tesla data, we observe that the difference is temperature dependent with a maximum at $T \approx 292$ K, implying that the structural transition is field-dependent, as suggested earlier by the thermal expansion measurements of Reuvekamp *et al.* Reuvekamp *et al.* (2014).

4) The elastic response of $EuTi_{0.95}Nb_{0.05}O_3$ does not show an observable magnetic field dependence in fields up to 3 Tesla.

Table 5.2 shows the T_S, density ρ, and the values of the elastic moduli for various samples. The data for single crystal of STO is obtained from the present RUS study. It can be clearly seen that the absolute values of the moduli for STO and ETO are very close.

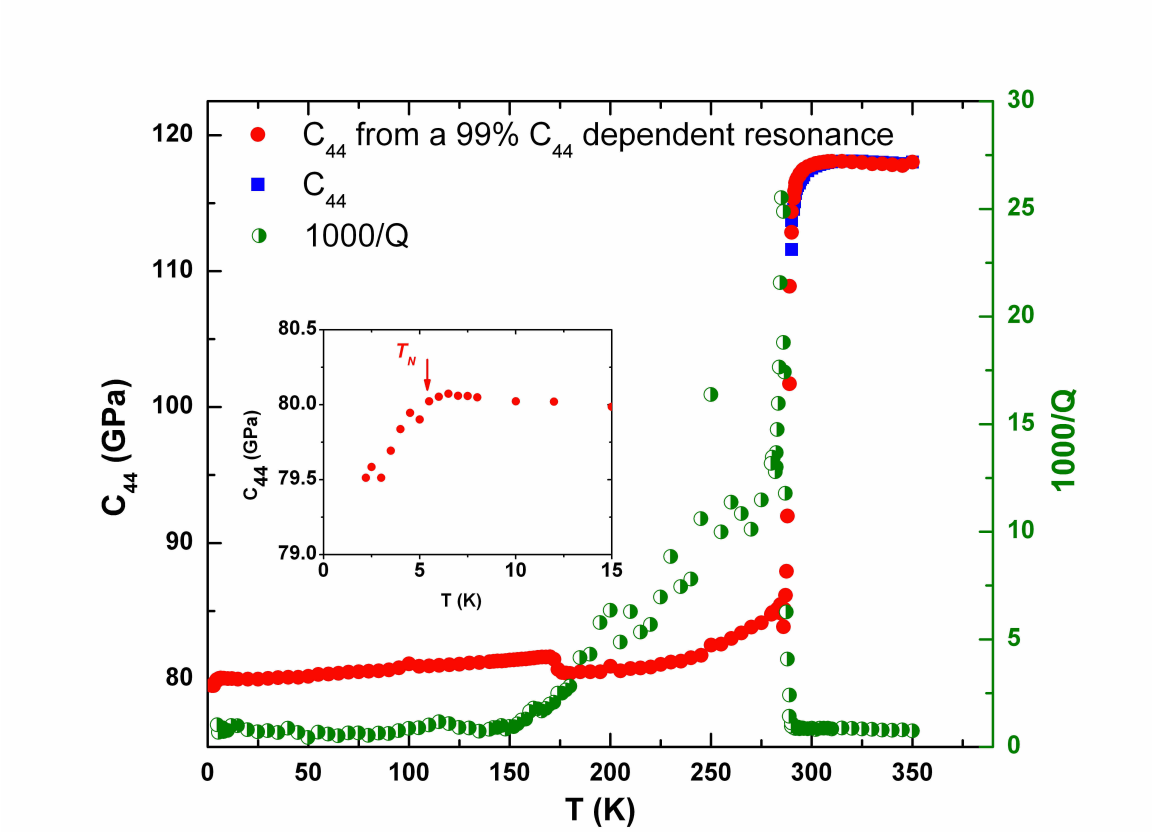

Figure 5.5: Temperature dependence of the shear modulus C_{44} and the inverse of the quality factor Q, which is defined as the center frequency of the resonance divided by full width at half maximum, of an oriented ETO single crystal. Note that below the structural phase transition temperature, C_{44} is determined directly from the first resonance peak (the red circle).

Figure 5.7 shows the temperature dependence of C_{44} for polycrystalline samples of $EuTi_{1-x}Nb_xO_3$ (x = 0, 0.03, 0.05, 0.1, 0.2 and 0.3). Because the porosity of the ceramic sample changes the density, and therefore the absolute value of the elastic moduli, we are only interested in the qualitative behavior, and to improve clarity the curves are offset along the y axis. The structural phase transition in $EuTi_{1-x}Nb_xO_3$ is marked by a step-like softening, which is significantly smeared out due to the presence of grains in polycrystalline samples. However, the trend that is clearly observed from

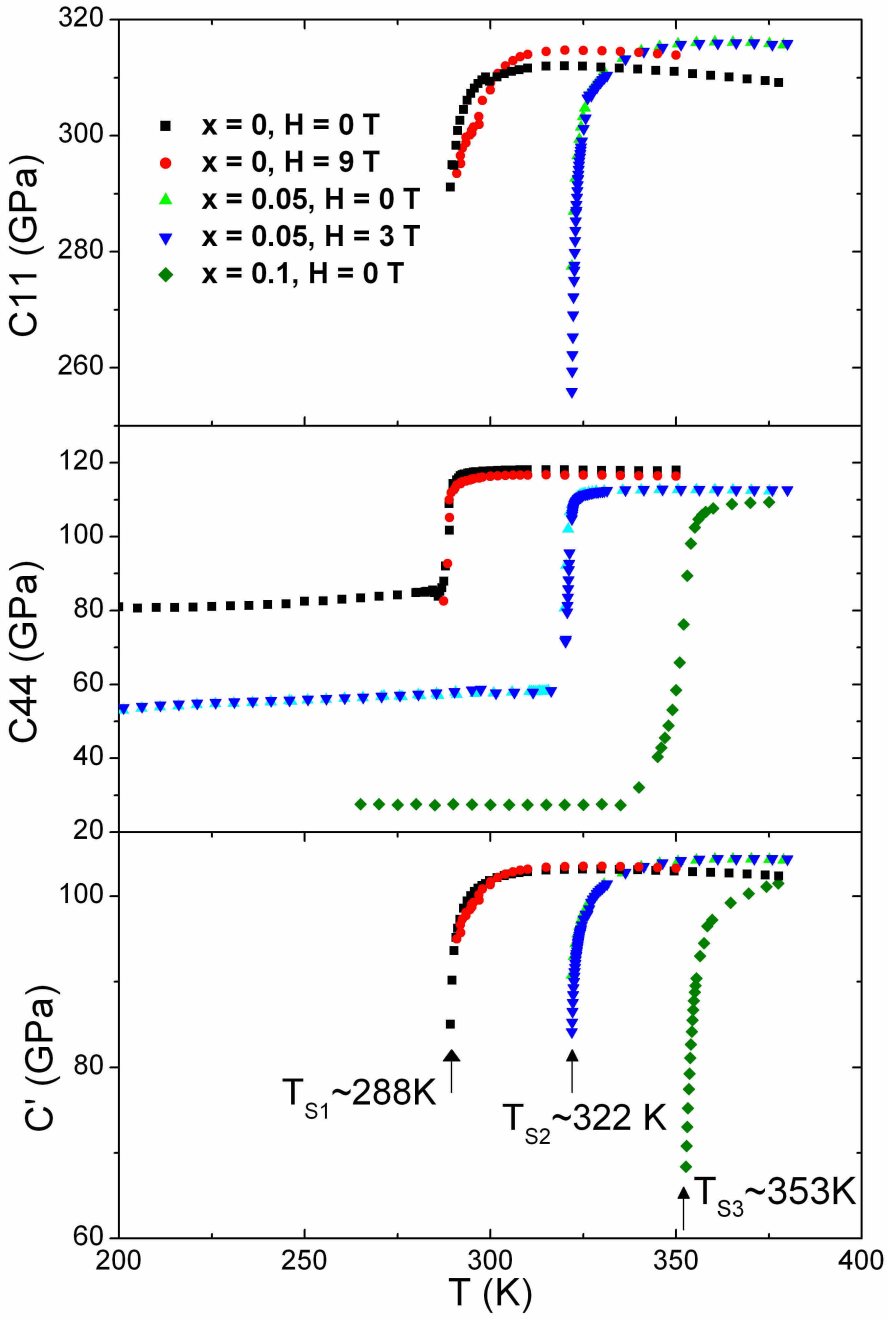

Figure 5.6: Temperature dependence of elastic constants for single crystal $EuTi_{1-x}Nb_xO_3$ (x=0, 0.05, and 0.1) in different magnetic fields. Measurements were performed during cooling.

Fig. 7 is that T_S increases with increasing Nb concentration and goes beyond our experimental range of 380 K when x reaches 0.2.

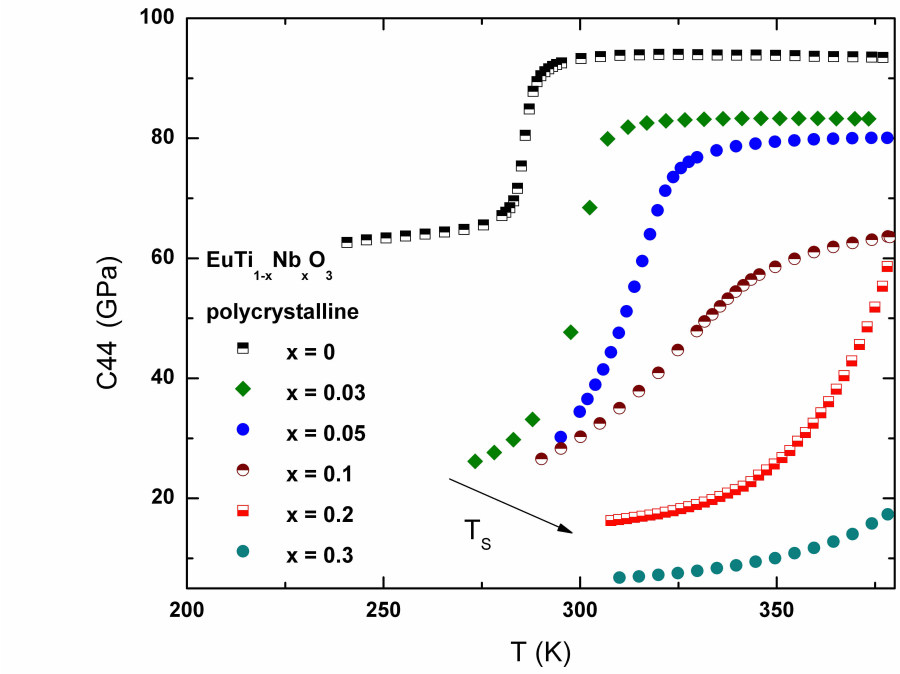

Figure 5.7: Temperature dependence of the shear modulus C_{44} for polycrystalline $EuTi_{1-x}Nb_xO_3$ (x=0, 0.03, 0.05, 0.1, 0.2, and 0.3). Data are shifted for clarity. Measurements were performed during cooling.

To compare the effect of Nb doping and Zr doping on the SPT of ETO, we have also performed RUS measurements on single crystals of $EuTi_{1-x}Zr_xO_3$ (x = 0, 0.005, and 0.015). Figure 5.8 presents the variation of shear modulus C_{44} with temperature for $EuTi_{1-x}Zr_xO_3$ (x=0, 0.005, and 0.015) single crystals. It can be clearly seen that all the three compositions present elastic softening with decreasing temperature, implying lattice instabilities. Nevertheless, the sharp step-like feature is actually absent for Zr-doped ETO crystals and the softening is significantly broadened. Intriguingly, the softening for x = 0.005 sample actually starts at a lower temperature

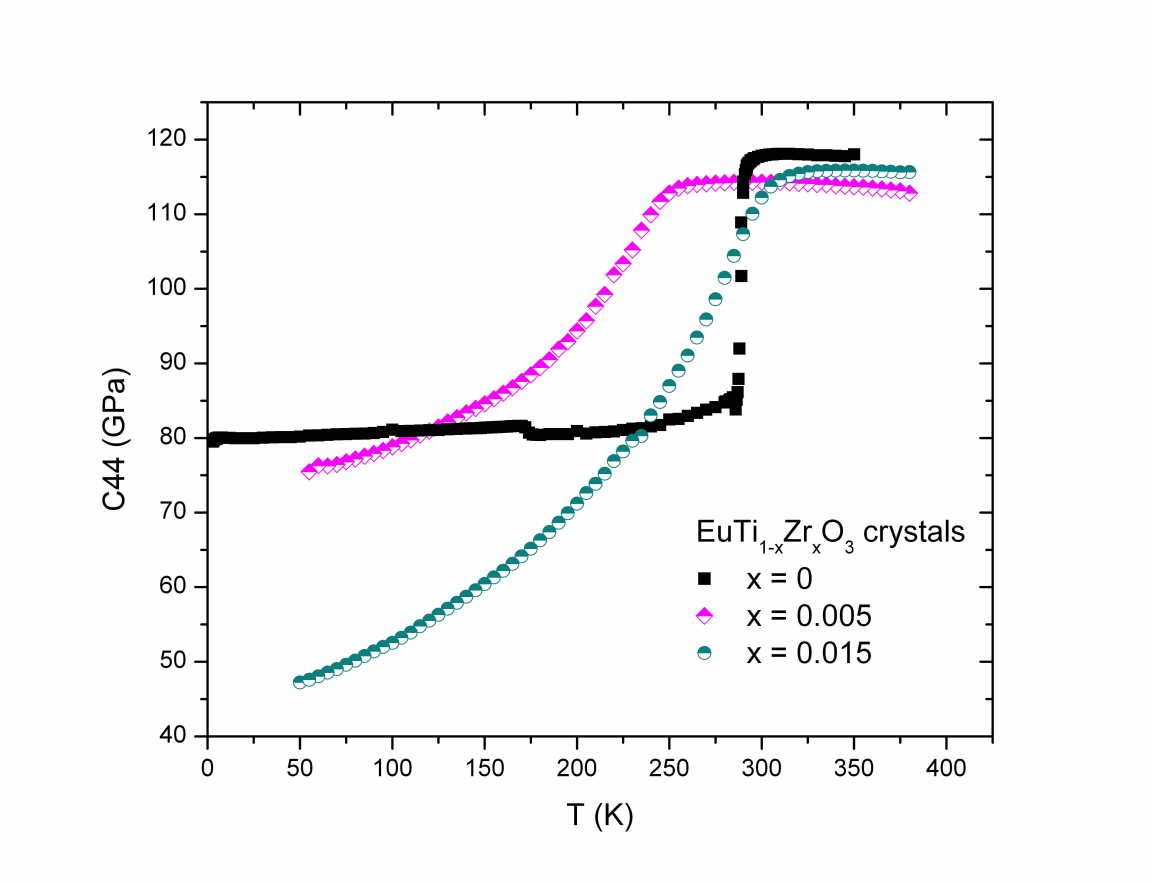

Figure 5.8: Temperature dependence of shear modulus C_{44} for single crystal $EuTi_{1-x}Zr_xO_3$ (x=0, 0.005, and 0.015). Measurements were performed during cooling.

of approx. 250 K compared to $T_S \approx 288$ K for ETO. With increasing Zr concentration, the softening takes place at a higher temperature of approx. 320 K ($x = 0.015$).

5.4 Discussion

5.4.1 Landau theory

As mentioned before, the elastic behavior of a material without any thermodynamic "anomalies" can be modeled using the so-called Varshni function Varshni (1970)

$$C_{ij}(T) = C_{ij}^0 - \frac{s}{e^{t/T} - 1} \tag{5.1}$$

which predicts a gradual stiffening with decreasing temperature that levels off at low temperatures. The elastic behavior of pure ETO obviously deviates from Varshni-behavior.

Landau theory is known to provide a proper framework for a formal analysis of phase transitions Rehwald (1973), whereby the free energy can be expressed in terms of strain e_i and order parameter components Q_i. Slonczewski *et al.* Slonczewski & Thomas (1970) performed a Landau analysis of the elastic behavior of $SrTiO_3$ in the 1970s, and here we present calculations using the Landau model for the $EuTiO_3$ system, adapting some of the notations used in Slonczewski & Thomas (1970). Note that inelastic X-ray scattering has indentified zone boundary R-point q=(0.5 0.5 0.5) acoustic phonon softening at this SPT Ellis *et al.* (2012). Thus the amplitudes of the degenerate zone boundary soft acoustic modes Q_1, Q_2, Q_3 can be naturally employed as the order parameter. Considering the crystal symmetry, the free energy F should include an antiferrodistortive energy $F(Q_1, Q_2, Q_3)$, the elastic energy $F(e)$, and a contribution from coupling between the order parameter and strain $F(Q, e)$:

$$F(Q_1, Q_2, Q_3) = A_1(Q_1^2 + Q_2^2 + Q_3^2) + A_2(Q_1^2 + Q_2^2 + Q_3^2)^2 + A_3(Q_1^2Q_2^2 + Q_2^2Q_3^2 + Q_3^2Q_1^2) \quad (5.2)$$

$$F(e) = \frac{1}{2}C_{11}^c(e_1^2 + e_2^2 + e_3^2) + C_{12}^c(e_1e_2 + e_2e_3 + e_3e_1) + \frac{1}{2}C_{44}^c(e_4^2 + e_5^2 + e_6^2) \quad (5.3)$$

$$F(Q,e) = -B_1(e_1Q_1^2 + e_2Q_2^2 + e_3Q_3^2) \\ - B_2(e_1(Q_2^2+Q_3^2) + e_2(Q_1^2+Q_3^2) + e_3(Q_1^2+Q_2^2)) \\ - B_t(e_4Q_2Q_3 + e_5Q_3Q_1 + e_6Q_1Q_2) \quad (5.4)$$

Here C_{11}^c, C_{12}^c and C_{44}^c are elastic moduli in the cubic phase, A_1, A_2, A_3 are Landau expansion coefficients, and B_1, B_2, B_t are coupling constants.

Assuming that the volume strain does not couple to the order parameter, this gives

$$B_e \equiv -B_2 = +B_1 \quad (5.5)$$

Under the equilibrium conditions $\frac{dF}{dQ} = 0$, $\frac{dF}{de} = 0$ this gives

$$e_i = \frac{B_e(3Q_i^2 - Q^2)}{C_{11}^c - C_{44}^c}(i = 1,2,3; Q^2 = Q_1^2 + Q_2^2 + Q_3^2), e_4 = \frac{B_t Q_2 Q_3}{C_{44}^c}, etc \quad (5.6)$$

The elastic constants are the second derivatives of the free energy F with respect to strain and may be calculated using the Slonczewski-Thomas formalism Slonczewski & Thomas (1970)

$$C_{ij} = C_{ij}^c - M^{-1}\sum_k \frac{\partial^2 F}{\partial e_i \partial Q_k}{\omega_k}^{-2}\frac{\partial^2 F}{\partial Q_k \partial e_j} \quad (5.7)$$

Substituting (2) $\rightarrow$ (6) into (7) and assuming $Q = (0,0,Q_s)$, we obtain the elastic moduli in the tetragonal phase:

$$C_{11} = C_{11}^c - D$$
$$C_{44} = C_{44}^c - E$$
$$C_{12} = C_{12}^c - D$$
$$C_{33} = C_{11}^c - 4D$$
$$C_{13} = C_{12}^c + 2D$$
$$C_{66} = C_{44}^c$$

where $D = (4B_e^2Q_s^2)/(M{\omega_3}^2)$, and $E = (B_t^2Q_s^2)/(M{\omega_2}^2)$. M is the mass density of the oxygen atoms participating in each optical vibration mode, and ω_i (i=1,2,3) are the natural frequencies of these vibration modes. Thus, as the cubic to tetragonal SPT is approached, a step-like softening is expected in the elastic moduli C_{11}, C_{12}, C_{44}, C_{33}, step-like stiffening is expected for C_{13}, and C_{66} is expected to follow the trend of the cubic shear modulus C_{44}. The step-like softening is clearly observed for C_{44} (Fig. 5), and even though the large absorption below T_S prevents us from determining the full elastic tensor below the transition, the precipitous drop in C_{11} and C' strongly suggests that these moduli undergo a similar step-like softening. While our Landau analysis predicts such behavior for the longitudinal modulus C_{11}, $C' = \frac{1}{2}(C_{11} - C_{12})$ is expected to smoothly continue through the SPT. This is clearly not observed. Interestingly, the same discrepancy is found in STO Bell & Rupprecht (1963b), and remains unexplained.

5.4.2 Precursor effect

In every aspect, the elastic response of ETO through the SPT appears to be very similar to that of STO, which is not surprising in light of the resemblance between their phonon behaviors Shirane & Yamada (1969); Ellis *et al.* (2012). The SPT

in both STO and ETO is driven by a condensation of zone-boundary phonon modes, which is indicative of the displacive nature of both SPTs. From a lattice dynamics point of view, precursor effects have been observed in STO by birefringence measurements Roleder *et al.* (2012), where fluctuating ferroelastic clusters form above T_S. Nevertheless, the TA-TO mode coupling which exists in STO and explains its precursor effects, is actually absent in ETO Bettis *et al.* (2011). The large neutron absorption inherent to Eu and the difficulty in growing large ETO crystals significantly hamper inelastic neutron experiments and further information regarding the phonon behavior has not yet been obtained. However, our observation of a gentle rounding rather than a sharp step in C_{ij} indicates that the precursor effect takes place in ETO starting about 20 K above T_S, where local elastic nanoregions develop. This is consistent with the pair distribution analysis Allieta *et al.* (2012) that showed that the dynamic fluctuations occur above T_S, *i.e.* tetragonal twinning segments form along three crystallographic orientations. This unexpected precursor effect in ETO has been analyzed by normalizing the transverse modes and taking the derivatives of the modes with respect to momentum, yielding the softening of the transverse acoustic mode as a function of temperature Bussmann-Holder *et al.* (2015). The coupling between the TA mode and the elastic constants gives rise to the elastic softening as the SPT is approached. Furthermore, the presence of the precursor effect suggests that the transition is not purely of the displacive type, but includes elements of an order/disorder transition.

5.4.3 Doping Effects

Figure 5.9 presents the $EuTi_{1-x}Nb_xO_3$ phase diagram with the structural and magnetic transition temperatures as a function of Nb content (T_N for $x = 0.015$, 0.03 and T_C for $x \geq 0.3$ samples are taken from Ref. Li *et al.* (2014)). The magnetic ground state changes from AFM to FM when $x \geq 0.1$. While T_N gradually decreases from 5.7 K ($x = 0$) to 4.5 K ($x = 0.05$), T_C increases slightly from 8.2 K ($x = 0.1$) to a

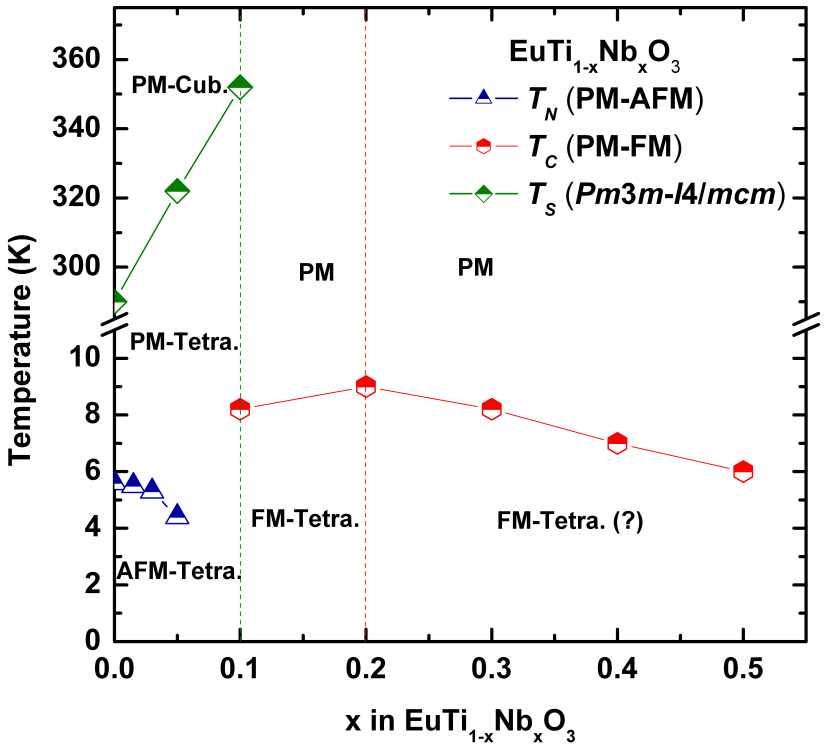

Figure 5.9: The temperature of the structural and magnetic phase transition *vs.* Nb content x in $EuTi_{1-x}Nb_xO_3$.

maximum of 9.3 K ($x = 0.2$), and decreases with further Nb doping. Structurally, Nb doping enhances T_C from 288 K ($x = 0$) to 353 K ($x = 0.1$). Nevertheless, the lattice distortion at 100 K is weakened with increasing Nb content. The well established tolerance factor t concept predicts the symmetry of ABO_3 perovskites structure, with $t = \frac{r_A + r_O}{\sqrt{2}(r_B + r_O)}$, and r_A, r_B, and r_O are the ionic radii of each ion. The radius of Nb^{4+} ($r = 0.68$ Å) is greater than that of Ti^{4+} ($r = 0.605$ Å) Shannon (1976), which means that substituting Nb for Ti reduces the tolerance factor and promotes the oxygen rotating instabilities. This is in favor of the cubic to tetragonal transformation occurring at higher temperatures with increasing Nb doing, as confirmed by RUS results. Nevertheless, this tolerance factor model, exclusively based on ion sizes, becomes problematic in an attempt to explain the difference in T_S between STO and

ETO. Neither does it explain the weaker octahedral distortion in $EuTi_{1-x}Nb_xO_3$ with increasing Nb concentration. It has been suggested that the high T_S of ETO compared to STO is associated with the hybridization between Eu f states and Ti d orbitals, which is also believed to be the origin of the giant spin-lattice coupling present in ETO Akamatsu *et al.* (2013). Previous studies have shown that Nb doping enhances T_S of STO to higher temperatures due to the local changes in the hybridization between the (Ti, Nb)-d orbitals and O-$2p$ orbitals Buerle & Rehwald (1978). Another important factor is the covalency of the transition metal-oxygen bond Garcia-Fernandez *et al.* (2010); Cammarata & Rondinelli (2014). Ab initio calculations have shown that the octahedral tilting angle in KMF_3 (M = transition metal) decreases linearly with the electron occupancy of the π-bonding t_{2g} orbitals of the transition metal. In the present system, Ti^{4+} has a $3d^0$ configuration. In contrast, Nb^{4+} possesses one electron in the t_{2g} orbitals, which most likely alters the covalency of the (Ti,Nb)-O bond and results in a weaker lattice distortion at low temperatures. It is noteworthy that $EuNbO_3$ is reported to remain cubic at room temperature, and octahedral tilting does not occur Zubkov *et al.* (1995b).

5.5 Summary

In this chapter, we have investigated the structural and magnetic transitions in both polycrystalline and single crystal samples of $EuTi_{1-x}Nb_xO_3$ ($0 \leq x \leq 0.3$) using synchrotron powder XRD, resonant ultrasound spectroscopy, and magnetization measurements. The cubic ($Pm\bar{3}m$) to tetragonal ($I4/mcm$) structural phase transition in pure and doped $EuTiO_3$ is characterized by a step-like elastic softening in C_{44}, C_{11}, and $C' = \frac{1}{2}(C_{11} - C_{12})$. Nb substitution for Ti significantly enhances T_S to higher temperatures ($T_S = 322$ K and 353 K for $EuTi_{0.95}Nb_{0.05}O_3$ and $EuTi_{0.9}Nb_{0.1}O_3$, respectively). In contrast, the octahedral tilting angle decreases with increasing Nb doping, which is possibly caused by the introduction of t_{2g} electrons on the Ti site. In the meanwhile, the introduction of itinerant t_{2g} electrons also switches

the magnetic ground state of $EuTiO_3$ from AFM to FM. Our study emphasizes the important role of the covalency of the transition metal - oxygen bond in determining the octahedral tilting amplitude and magnetic ground state in the present system. Band structure calculations of $EuTi_{1-x}Nb_xO_3$ will be useful to further examine how the hybridization between the Eu-f, (Ti,Nb)-d and O-p orbitals changes with electron doping concentration on the transition metal site.

Chapter 6

Magnetoelastic coupling in A_2FeReO_6 (A = Ba and Ca) probed by elastic constants and magnetostriction measurements

In this chapter, we discuss the magnetoelastic coupling effect in Ba_2FeReO_6 and Ca_2FeReO_6. Double perovskites A_2FeReO_6 (A = Ba, Ca) have been synthesized and studied using resonant ultrasound spectroscopy, magnetization, and magnetostriction measurements. A large softening in C_{44} over a wide temperature range is observed for Ba_2FeReO_6 below its Curie temperature ($T_C \approx 311$ K), which is indicative of a structural distortion. This softening is suppressed upon the application of a very low magnetic field. For Ca_2FeReO_6, both the longitudinal and shear moduli show a softening starting at $T \approx 160$ K. In addition, magnetoelastic coupling constants have been estimated from elastic constants and magnetostriction data, which provide direct evidence of pronounced coupling between magnetism and the lattice degrees of freedom present in both compounds.

A similar version of this chapter is published as L. Li, M. R. Koehler, I. Bredeson, J. He, D. Mandrus and V. Keppens, J. Appl. Phys. **117**, 213913 (2015).

6.1 Introduction

Double perovskites $A_2BB'O_6$ provide a wide range of new materials due to the plethora of elemental combinations on the B and B' sites, and exhibit versatile physical properties, including room temperature magnetoresistance Kobayashi *et al.* (1998) and magnetic frustration Aczel *et al.* (2013). Interest in Re-based double perovskites (B' = Re) stems from their high Curie temperature, high spin polarization, and large magneto-resistance, making them attractive candidates for industrial applications (see review article Serrate *et al.* (2007)). Among them, Sr_2CrReO_6 is shown to possess the highest $T_C \approx 635$ K Kato *et al.* (2002b). Ba_2FeReO_6 (BFRO) is a ferrimagnetic metal with mixed valence states of Fe^{2+}/Re^{6+} and Fe^{3+}/Re^{5+} (reference Sleight & Weiher (1972)). BFRO was believed to remain cubic $Fm\bar{3}m$ at all temperatures, but a detailed structural study using high-intensity synchrotron radiation recently detected a slight lattice distortion below $T_C \approx 315$ K Ferreira *et al.* (2006). In contrast, Ca_2FeReO_6 (CFRO) is a monoclinic Mott insulator and orders ferrimagnetically below $T_C \approx 521$ K Granado *et al.* (2002). The symmetry loss from A= Ba to A=Ca can be understood by taking into account that a smaller cation size favors the tilting of the Fe/ReO_6 octahedra. CFRO has received extra attention due to the following discoveries: 1) it exhibits giant anisotropic magnetostriction effect Serrate *et al.* (2005), which makes it attractive in the field of spin electronics; 2) it goes through a coupled structural, magnetic, and metal-insulator transition between 135 and 150 K Granado *et al.* (2002); Kato *et al.* (2002a); Westerburg *et al.* (2002); Oikawa *et al.* (2003). In this Chapter, we present measurements of elastic constants, magnetization and magnetostriction on polycrystalline BFRO and CFRO. The results provide direct evidence for a large magnetoelastic coupling present in both compounds.

6.2 Experimental details

Polycrystalline samples of BFRO and CFRO have been synthesized by solid state reaction as described in Chapter 3. Both compounds yield well-crystallized black powders. Powder X-ray diffraction patterns were recorded using a D2 Phaser with CuK_α radiation at room temperature. Both compounds are single phase. The samples were spark plasma sintered and cut into rectangular parallelepipeds with dimensions of the order of a few millimeters for resonant ultrasound spectroscopy (RUS) measurements. The RUS data reported here were carried out as a function of temperature (50 to 380 K) and magnetic field (0 to 2 Tesla) using a custom designed probe that was inserted in a commercial Quantum Design Versalab system. The *dc* magnetic susceptibility measurements were carried out using a Quantum Design Versalab system with a vibrating sample magnetometer (VSM) after cooling in either zero field (ZFC) or in a measuring field (FC) of 1000 Oe. Magnetostriction measurements as a function of field (0 to 3 T) and temperature (50 to 380 K) have been performed using the capacitance dilatometer as described in Chapter 3.

6.3 Results and Discussion

Figure 6.1(a) presents the magnetic susceptibility of BFRO, plotted as both χ and $1/\chi$. This compound shows a ferrimagnetic ordering at $T_C \approx 311$ K, that is in good agreement with previous work Sleight & Weiher (1972). Polycrystalline materials are elastically isotropic and have only two independent elastic moduli: the shear modulus C_{44} (or G) and the longitudinal modulus C_{11} (or L). They are related to the shear and longitudinal sound waves traveling along [100] directions through $v_{(S,L)} = (\frac{C_{(44,11)}}{\rho})^{\frac{1}{2}}$. The shear modulus C_{44} *vs.* T and longitudinal modulus C_{11} *vs.* T are plotted in Figure 6.1(b) and (c). It should be noted that C_{11} for this sample is not well-defined as most resonant frequencies depend entirely on the shear modulus. As mentioned before, the elastic moduli of materials with no thermodynamic irregularities are known to

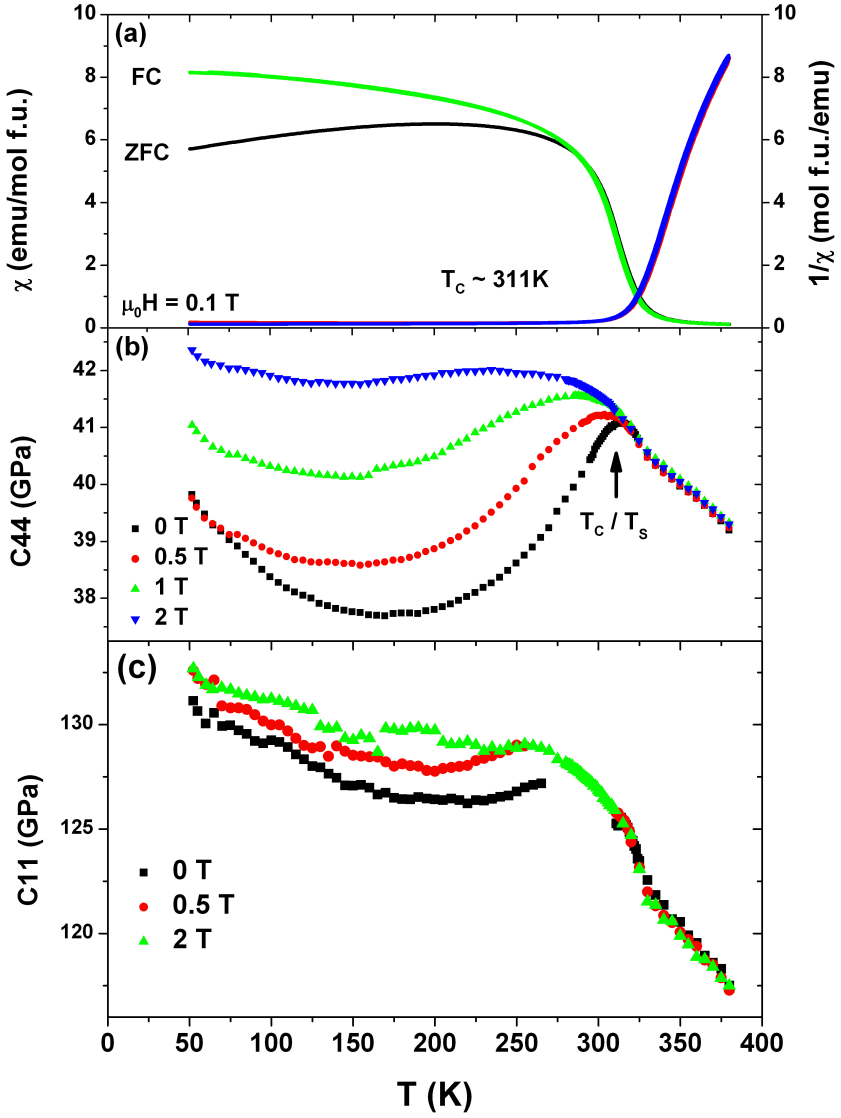

Figure 6.1: Temperature dependence of (a) *dc* magnetization at 0.1 T, (b) shear modulus C_{44} at different magnetic fields, and (c) longitudinal modulus C_{11} at different magnetic fields for polycrystalline Ba_2FeReO_6. RUS measurements were performed during cooling.

exhibit the so-called Varshni behavior Varshni (1970), with a gradual stiffening with decreasing temperature that levels off at very low temperatures. Intriguingly, one can see that C_{44} presents a pronounced softening of almost 10 % that spans a wide temperature range below T_C. Such a dramatic softening is usually associated with structural phase transitions. While this compound was believed to remain cubic at all

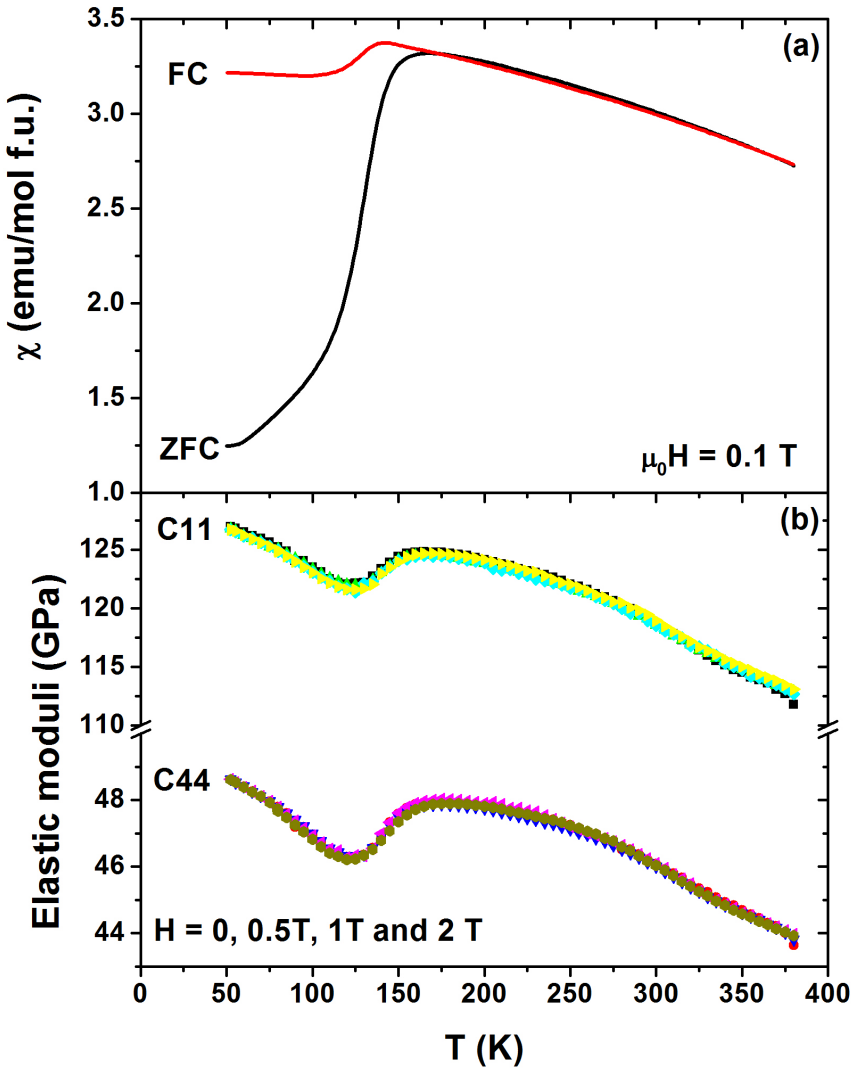

Figure 6.2: Temperature dependence of (a) *dc* magnetization at 0.1 T, (b) longitudinal modulus C_{11} and shear modulus C_{44} at differnet magnetic fields for polycrystalline Ca_2FeReO_6. RUS measurements were performed during cooling.

temperatures, a recent structural study utilizing high resolution powder diffraction reports a subtle lattice distortion driven by the rotation of the octahedra Ferreira *et al.* (2006). It is therefore tempting to link the observed softening to the structural distortion below $T_C \approx 311$ K. The softening is greatly suppressed upon the application of a magnetic field, which would indicate that the lattice distortion is weakened by the magnetic field. However, it is noteworthy that many ferro(ferri)magnetic materials

exhibit the so-called ΔE-effect, which manifests itself in a sudden softening of the elastic moduli at T_C, which is suppressed upon application of a magnetic field Siegel & Quimby (1936). At this time, it is not possible to determine whether the softening observed in BFRO is attributed to the structural distortion or the ΔE effect, and high-intensity X-ray diffraction measurements in magnetic field might be required to resolve this issue.

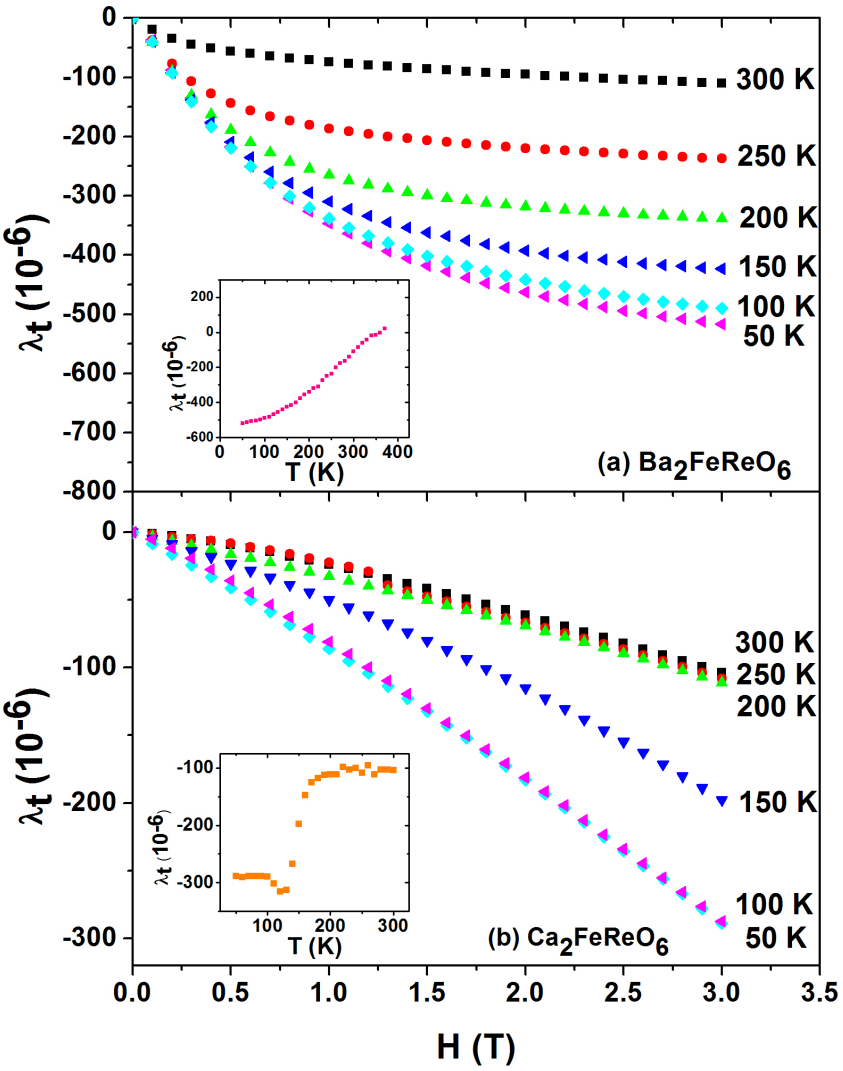

Figure 6.3: Variation of anisotropic magnetostriction λ_t with magnetic field H at different temperatures for (a) Ba_2FeReO_6 and (b) Ca_2FeReO_6. The insets present λ_t vs. T at 3 Tesla for each compound.

Figure 6.2 shows the temperature dependence of (a) magnetic susceptibility under ZFC and FC conditions, and (b) C_{44} and C_{11} under different magnetic fields (0, 0.5, 1, and 2 Tesla) for CFRO. CFRO orders ferrimagnetically at a very high temperature of $T_C \approx 521$ K. Elastic softening can be observed below $T \approx 160$ K, which is associated with a simultaneous occurrence of structural, orbital and metal-insulator transitions Granado *et al.* (2002); Kato *et al.* (2002a); Westerburg *et al.* (2002); Oikawa *et al.* (2003). In contrast to BFRO, the magnetic behavior of CFRO is not sensitive to magnetic fields up to 2 Tesla.

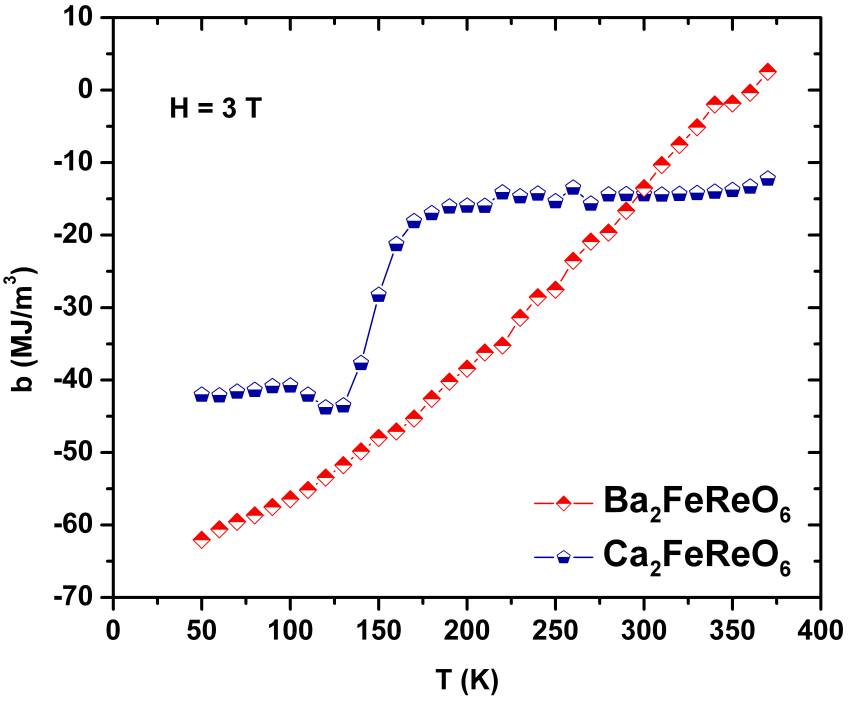

Figure 6.4: Temperature dependence of the magnetoeleastic coupling constant b for Ba_2FeReO_6 and Ca_2FeReO_6.

Magnetostriction is a property of ferromagnetic materials that causes the material to change dimensions during magnetization. In order to estimate the interaction between lattice and magnetic degrees of freedom, we have performed magnetostriction measurements on RUS samples of BFRO and CFRO. Figure 6.3 presents the

anisotropic magnetostriction λ_t *vs.* H up to 3 Tesla at different temperatures. λ_t is defined as: $\lambda_t = \lambda_{\parallel} - \lambda_{\perp}$ with $\lambda_{\parallel}$ the relative change in length in the direction of the applied field, and $\lambda_{\perp}$ the relative change in length perpendicular to the applied field. One can see that within our experimental range of 3 Tesla, BFRO shows a greater magnetostriction than CFRO. Nevertheless, the saturation field of BFRO is much lower than that of CFRO. In fact, giant magnetostriction measurements performed under magnetic fields up to 20 T have shown that λ_t saturates at H $\approx$ 15 T and reaches a maximum value of $\approx$ 600 ppm for CFRO Serrate *et al.* (2005). Our results show that λ_t of BFRO reaches $\approx$ 520 ppm and one can conclude that the magnitude of magnetostriction is comparable for BFRO and CFRO, which is not surprising since both compounds possess significant spin-orbital coupling arising from the Re $5d$ t_{2g} electrons. The insets show the temperature dependence of λ_t at 3 T for BFRO and CFRO respectively. While the absolute value of λ_t for BFRO increases continuously with dropping temperature, that of CFRO shows a dramatic rise near T_S that is possibly associated with the change of electronic structure.

Given the polycrystalline elastic moduli and magnetostriction data, the magnetoelastic coupling constant b can be determined assuming the magnetization is saturated:

$$b = \frac{\Delta l}{l}(2 * C_{44})(\alpha^2 - \frac{1}{3})^{-1} \tag{6.1}$$

Here, b is the magnetoelastic coupling constant and α is the cosine of the angle between the magnetization and measuring direction, which is equal to 1 since we assumed that the magnetization is saturated (note that this estimate will yield an under-estimated value for b as saturation is clearly not reached in CFRO). Using the $\frac{\Delta l}{l}$ values at 3 Tesla, the calculated values of b are presented in Figure 6.4. The magnitude of b for BFRO and CFRO are similar. Similar to λ_t, it is clearly shown that b of CFRO presents a step-like drop near T_S, which is likely correlated with simultaneous metal-insulator, magnetic and structural transitions.

6.4 Summary

In this Chapter, we synthesized and investigated the magnetoelastic coupling in polycrystalline Ba_2FeReO_6 and Ca_2FeReO_6 with combined measurements of elastic constants, magnetization and magnetostriction. A large softening in C_{44} over a wide temperature range is observed for Ba_2FeReO_6 below $T_C \approx 311$ K, which is partially suppressed upon application of a magnetic field. This softening is associated with a coupled structural and ferrimagnetic transition. For Ca_2FeReO_6, the elastic softening spans a narrower temperature range, and is not sensitive to magnetic fields up to 2 Tesla. This softening is related to a metal - insulator transition accompanied by an octahedral distortion, which also promotes the occurrence of orbital ordering of the Re $5d$ t_{2g} electrons. Significant magnetostriction has been observed in both compounds. Our results provide direct evidence of correlated interactions between spin, lattice and orbital degrees of freedom in these two compounds.

Chapter 7

Concluding remarks

Multiferroics with strong coupling between magnetic, electrical and orbital degrees of freedom are rare. An understanding of the interplay between these degrees of freedom will allow for the realization of controlling electrical polarization through magnetization or vice versa and therefore greatly advance the field of spintronic devices.

Bulk $EuTiO_3$ is a quantum paraelectric antiferromagnet with a strong magnetoelectric coupling as revealed in a pronounced decrease of the dielectric constant at $T_N \approx 5.6$ K Katsufuji & Takagi (2001). The observation of simultaneous ferroelectric and ferromagnetic ordering in strained $EuTiO_3$ further confirms the multiferroic potential of this material Lee *et al.* (2010). Very recently, a structural phase transition (SPT) was observed in $EuTiO_3$ at $T \approx 282$ K in heat capacity experiment Bussmann-Holder *et al.* (2011), generating some controversies regarding T_S and the existence of incommensurate structure below T_S. Motivated by these results, we have initiated a study of the elastic, structural, magnetic, and transport properties of $EuTiO_3$ single crystals as well as mixed crystals of $EuTi_{1-x}B_xO_3$ (B = Zr, Nb). The antiferrodistortive SPT in $EuTiO_3$ is confirmed in resonant ultrasound spectroscoy measurement and is characterized by a step-like elastic softening in a narrow temperature interval in the vicinity of $T_S \approx 288$ K. Our RUS results suggests

that Nb doping enhances T_S to higher temperatures, while the octahedral tilting is weakened, as evidenced by synchrotron XRD. Magnetic measurements confirm that Nb doping destabilizes the antiferromagnetic ground state of the parent compound and long range ferromagnetic order is observed in the samples containing more than 5 % Nb, which is most likely accounted for in terms of the ferromagnetic interaction between localized Eu $4f$ spins mediated by itinerant electrons introduced by Nb doping. However, Nb doping converts the system to metallic due to the d^1 configuration of Nb^{4+}.

Divalent Eu compounds are being studied extensively, but present an additional challenge due to the difficulty in maintaining the right valence state. While EuO exhibit FM ordering, $EuTiO_3$, on the other hand, presents a G-type AFM ordering. The complex magnetic interactions in divalent Eu compounds deserve further investigation. Note that $EuGeO_3$ and $EuSiO_3$ has been predicted to exhibit ferromagnetic ordering Akamatsu *et al.* (2011) due to the positive value of J_1 for nearest neighbor interactions. The Ruddlesden-Popper phase Eu_2TiO_4 with alternating EuO and $EuTiO_3$ layers also exhibits a ferromagnetic ground state below $T_C \approx 7.8$ K Chien *et al.* (1974); Greedan & McCarthy (1972). Those are attractive candidates in the search for materials with large magnetoelectric coupling and/or multiferroic materials.

Bibliography

Aczel, A. A., Bugaris, D. E., Li, L., Yan, J.-Q., de la Cruz, C., zur Loye, H.-C., & Nagler, S. E. 2013. Frustration by competing interactions in the highly distorted double perovskites $La_2NaB'O_6$ (B' = Ru, Os). *Phys. Rev. B*, **87**(Jan), 014435. 67

Akahoshi, Daisuke, Horie, Hiroki, Sakai, Shingo, & Saito, Toshiaki. 2013. Ferromagnetic behavior in mixed valence europium (Eu2+/Eu3+) oxide $EuTi_{1-x}M_xO_3$ (M=Al3+ and Ga3+). *Appl. Phys. Lett.*, **103**(17), 172407. 35

Akamatsu, Hirofumi, Kumagai, Yu, Oba, Fumiyasu, Fujita, Koji, Murakami, Hideo, Tanaka, Katsuhisa, & Tanaka, Isao. 2011. Antiferromagnetic superexchange via 3*d* states of titanium in $EuTiO_3$ as seen from hybrid Hartree-Fock density functional calculations. *Phys. Rev. B*, **83**(Jun), 214421. 41, 76

Akamatsu, Hirofumi, Kumagai, Yu, Oba, Fumiyasu, Fujita, Koji, Tanaka, Katsuhisa, & Tanaka, Isao. 2013. Strong Spin-Lattice Coupling Through Oxygen Octahedral Rotation in Divalent Europium Perovskites. *Advanced Functional Materials*, **23**(15), 1864–1872. 42, 64

Allieta, Mattia, Scavini, Marco, Spalek, Leszek, Scagnoli, Valerio, Walker, Helen, Panagopoulos, Christos, Saxena, Siddharth, Katsufuji, Takuro, & Mazzoli, Claudio. 2012. Role of intrinsic disorder in the structural phase transition of magnetoelectric $EuTiO_3$. *Phys. Rev. B*, **85**(18), 1–8. 46, 49, 62

Bell, R. O., & Rupprecht, G. 1963a. Elastic Constants of Strontium Titanate. *Phys. Rev.*, **129**(Jan), 90–94. 2, 53

Bell, R. O., & Rupprecht, G. 1963b. Elastic Constants of Strontium Titanate. *Phys. Rev.*, **129**(Jan), 90–94. 61

Bessas, D., Rushchanskii, K. Z., Kachlik, M., Disch, S., Gourdon, O., Bednarcik, J., Maca, K., Sergueev, I., Kamba, S., Ležaić, M., & Hermann, R. P. 2013. Lattice instabilities in bulk $EuTiO_3$. *Phys. Rev. B*, **88**(14), 144308. 46

Bettis, Jerry L., Whangbo, Myung-Hwan, Köhler, Jürgen, Bussmann-Holder, Annette, & Bishop, A. R. 2011. Lattice dynamical analogies and differences between $SrTiO_3$ and $EuTiO_3$ revealed by phonon-dispersion relations and double-well potentials. *Phys. Rev. B*, **84**(18), 184114. 62

Birol, Turan, & Fennie, Craig J. 2013. Origin of giant spin-lattice coupling and the suppression of ferroelectricity in $EuTiO_3$ from first principles. *Phys. Rev. B*, **88**(Sep), 094103. 46, 47

Bruce, Alastair D., Müller, K. A., & Berlinger, W. 1979. Order-Disorder Behavior at Displacive Structural Phase Transitions. *Phys. Rev. Lett.*, **42**(Jan), 185–188. 46

Buerle, D., & Rehwald, W. 1978. Structural phase transitions in semiconducting $SrTiO_3$. *Solid State Communications*, **27**(12), 1343 – 1346. 64

Bussmann-Holder, A., Büttner, H., & Bishop, A. 2007. Polar-Soft-Mode-Driven Structural Phase Transition in $SrTiO_3$. *Phys. Rev. Lett.*, **99**(16), 1–4. 46

Bussmann-Holder, A., Köhler, J., Kremer, R., & Law, J. 2011. Relation between structural instabilities in $EuTiO_3$ and $SrTiO_3$. *Phys. Rev. B*, **83**(21), 1–4. 46, 75

Bussmann-Holder, Annette, Khler, Jrgen, & Whangbo, Mike-H. 2015. Unexpected Precursor Effects to the Structural Phase Transition in EuTiO3. *Zeitschrift fr anorganische und allgemeine Chemie*, **641**(2), 180–183. 62

Cammarata, Antonio, & Rondinelli, James M. 2014. Covalent dependence of octahedral rotations in orthorhombic perovskite oxides. *The Journal of Chemical Physics*, **141**, 114704. 64

Chien, Chia-Ling, DeBenedetti, S., & Barros, F. De S. 1974. Magnetic properties of $EuTiO_3$, Eu_2TiO_4, and $Eu_3Ti_2O_7$. *Phys. Rev. B*, **10**(Nov), 3913–3922. 76

Ellis, David S., Uchiyama, Hiroshi, Tsutsui, Satoshi, Sugimoto, Kunihisa, Kato, Kenichi, Ishikawa, Daisuke, & Baron, Alfred Q. R. 2012. Phonon softening and dispersion in $EuTiO_3$. *Phys. Rev. B*, **86**(Dec), 220301. 46, 47, 59, 61

Ellis, David S., Uchiyama, Hiroshi, Tsutsui, Satoshi, Sugimoto, Kunihisa, Kato, Kenichi, & Baron, Alfred Q.R. 2014. X-ray study of the structural distortion in $EuTiO_3$. *Physica B: Condensed Matter*, **442**(0), 34 – 38. 46, 47

Ferreira, Fabio Furlan, Granado, Eduardo, Carvalho Jr, Wilson, Kycia, Stefan W., Bruno, Daniele, & Droppa Jr, Roosevelt. 2006. X-ray powder diffraction beamline at D10B of LNLS: application to the Ba_2FeReO_6 double perovskite. *Journal of Synchrotron Radiation*, **13**(1), 46–53. 67, 70

Fleury, PA, Scott, JF, & Worlock, JM. 1968. Soft Phonon Modes and the 110 K Phase Transition in $SrTiO_3$. *Phys. Rev. Lett.*, **21**(1), 16. 46

Garcia-Fernandez, P., Aramburu, J. a., Barriuso, M. T., & Moreno, M. 2010. Key role of covalent bonding in octahedral tilting in perovskites. *Journal of Physical Chemistry Letters*, **1**, 647–651. 64

Glazer, A. M. 1972. The classification of tilted octahedra in perovskites. *Acta Crystallographica Section B Structural Crystallography and Crystal Chemistry*, **28**(11), 3384–3392. 6

Goian, V., Kamba, S., Pacherová, O., Drahokoupil, J., Palatinus, L., Dušek, M., Rohlíček, J., Savinov, M., Laufek, F., Schranz, W., Fuith, A., Kachlík, M.,

Maca, K., Shkabko, A., Sagarna, L., Weidenkaff, A., & Belik, A. A. 2012. Antiferrodistortive phase transition in $EuTiO_3$. *Phys. Rev. B*, **86**(Aug), 054112. 46, 47, 48

Granado, E., Huang, Q., Lynn, J. W., Gopalakrishnan, J., Greene, R. L., & Ramesha, K. 2002. Spin-orbital ordering and mesoscopic phase separation in the double perovskite Ca_2FeReO_6. *Phys. Rev. B*, **66**(Aug), 064409. 67, 72

Greedan, J.E., & McCarthy, Gregory J. 1972. Crystal chemistry and magnetic properties of Eu_2TiO_4 and $Eu_3Ti_2O_7$. *Materials Research Bulletin*, **7**(6), 531 – 541. 76

Guguchia, Z, Keller, H, Khler, J, & Bussmann-Holder, A. 2012. Magnetic field enhanced structural instability in $EuTiO_3$. *Journal of Physics: Condensed Matter*, **24**(49), 492201. 46

Guguchia, Z, Caslin, K, Kremer, R K, Keller, H, Shengelaya, A, Maisuradze, A, Jr, J L Bettis, Khler, J, Bussmann-Holder, A, & Whangbo, M-H. 2013. Nonlinear pressure dependence of T_N in almost multiferroic $EuTiO_3$. *Journal of Physics: Condensed Matter*, **25**(37), 376002. 43

Imada, Masatoshi, Fujimori, Atsushi, & Tokura, Yoshinori. 1998. Metal-insulator transitions. *Rev. Mod. Phys.*, **70**(Oct), 1039–1263. 46

Ishikawa, Kenji, ya Adachi, Gin, & Shiokawa, Jiro. 1983. Electrical properties of sintered $EuTiO_3$- $EuNbO_3$. *Materials Research Bulletin*, **18**(3), 257 – 262. 35, 43

Jahn, H. A., & Teller, E. 1937. Stability of Polyatomic Molecules in Degenerate Electronic States. I. Orbital Degeneracy. *Proceedings of the Royal Society of London A: Mathematical, Physical and Engineering Sciences*, **161**(905), 220–235. 13

Kato, H., Okuda, T., Okimoto, Y., Tomioka, Y., Oikawa, K., Kamiyama, T., & Tokura, Y. 2002a. Metal-insulator transition of ferromagnetic ordered double perovskites: $(Sr_{1-y}Ca_y)_2FeReO_6$. *Phys. Rev. B*, **65**(Mar), 144404. 67, 72

Kato, H., Okuda, T., Okimoto, Y., Tomioka, Y., Takenoya, Y., Ohkubo, A., Kawasaki, M., & Tokura, Y. 2002b. Metallic ordered double-perovskite Sr_2CrReO_6 with maximal Curie temperature of 635 K. *Appl. Phys. Lett.*, **81**(2). 3, 67

Katsufuji, T., & Takagi, H. 2001. Coupling between magnetism and dielectric properties in quantum paraelectric $EuTiO_3$. *Phys. Rev. B*, **64**(Jul), 054415. 2, 34, 46, 52, 75

Katsufuji, T., & Tokura, Y. 1999. Transport and magnetic properties of a ferromagnetic metal: $Eu_{1-x}R_xTiO_3$. *Phys. Rev. B*, **60**(Dec), R15021–R15023. 39, 43, 52

Kennedy, Brendan J, Murphy, Gabriel, Reynolds, Emily, Avdeev, Maxim, Brand, Helen E R, & Kolodiazhnyi, Taras. 2014. Studies of the antiferrodistortive transition in $EuTiO_3$. *Journal of physics. Condensed matter : an Institute of Physics journal*, **26**(49), 495901. 47

Kim, Jong-Woo, Thompson, Paul, Brown, Simon, Normile, Peter S., Schlueter, John a., Shkabko, Andrey, Weidenkaff, Anke, & Ryan, Philip J. 2013. Emergent Superstructural Dynamic Order due to Competing Antiferroelectric and Antiferrodistortive Instabilities in Bulk $EuTiO_3$. *Phys. Rev. Lett.*, **110**(2), 027201. 46

Kittle, Charles. 2005. *Introduction of Solid State Physics*. John Wiley and Sons, Inc. xiv, 24

Kobayashi, K.-I., Kimura, T., Sawada, H., Terakura, K., & Tokura, Y. 1998. Room-temperature magnetoresistance in an oxide material with an ordered double-perovskite structure. *Nature*, **395**(October), 677–680. 67

Kolodiazhnyi, T., Fujita, K., Wang, L., Zong, Y., Tanaka, K., Sakka, Y., & Takayama-Muromachi, E. 2010. Magnetodielectric effect in $EuZrO_3$. *Applied Physics Letters*, **96**(25), 252901. 35

Kugimiya, Kazuma, Fujita, Koji, Tanaka, Katsuhisa, & Hirao, Kazuyuki. 2007. Preparation and magnetic properties of oxygen deficient $EuTiO_{3-\delta}$ thin films. *Journal of Magnetism and Magnetic Materials*, **310**(2, Part 3), 2268 – 2270. 43

Kususe, Yoshiro, Murakami, Hideo, Fujita, Koji, Kakeya, Itsuhiro, Suzuki, Minoru, Murai, Shunsuke, & Tanaka, Katsuhisa. 2014. Magnetic and transport properties of $EuTiO_3$ thin films doped with Nb. *Japanese Journal of Applied Physics*, **53**(5S1), 05FJ07. 35, 43

Lee, June Hyuk, Fang, Lei, Vlahos, Eftihia, Ke, Xianglin, Jung, Young Woo, Kourkoutis, Lena Fitting, Kim, Jong-Woo, Ryan, Philip J, Heeg, Tassilo, Roeckerath, Martin, Goian, Veronica, Bernhagen, Margitta, Uecker, Reinhard, Hammel, P Chris, Rabe, Karin M, Kamba, Stanislav, Schubert, Jürgen, Freeland, John W, Muller, David a, Fennie, Craig J, Schiffer, Peter, Gopalan, Venkatraman, Johnston-Halperin, Ezekiel, & Schlom, Darrell G. 2010. A strong ferroelectric ferromagnet created by means of spin-lattice coupling. *Nature*, **466**(7309), 954–8. 2, 34, 43, 47, 75

Li, Ling, Zhou, Haidong, Yan, Jiaqiang, Mandrus, David, & Keppens, Veerle. 2014. Research Update: Magnetic phase diagram of $EuTi_{1-x}B_xO_3$ (B = Zr, Nb). *APL Materials*, **2**(11), 110701. 47, 52, 62

Luan, Yanbing, Keppens, Veerle, Jin, Rongying, & Mandrus, David. 2009. Resonant ultrasound studies of the layered perovskite system $Ca_{2-x}Sr_xRuO_4$. *The Journal of the Acoustical Society of America*, **126**(6). xiv, 28

Migliori, A., Sarrao, J.L., Visscher, William M., Bell, T.M., Lei, Ming, Fisk, Z., & Leisure, R.G. 1993. Resonant ultrasound spectroscopic techniques for measurement of the elastic moduli of solids. *Physica B: Condensed Matter*, **183**(12), 1 – 24. 1, 25, 29

Oikawa, Kenichi, Kamiyama, Takashi, Kato, Hisato, & Tokura, Yoshinori. 2003. Structural Distortion on MetalInsulator Transition in Ordered Double Perovskite Ca_2FeReO_6. *Journal of the Physical Society of Japan*, **72**(6), 1411–1417. 67, 72

Rehwald, W. 1973. The study of structural phase transitions by means of ultrasonic experiments. *Advances in Physics*, **22**(Nov.), 721–755. xiv, 31, 33, 59

Reuvekamp, Patrick G., Kremer, Reinhard K., Köhler, Jürgen, & Bussmann-Holder, Annette. 2014. Evidence for the first-order nature of the structural instability in $EuTiO_3$ from thermal expansion measurements. *Phys. Rev. B*, **90**(10), 104105. 54

Rodrguez-Carvajal, Juan. 1993. Recent advances in magnetic structure determination by neutron powder diffraction. *Physica B: Condensed Matter*, **192**(12), 55 – 69. 17, 36

Roleder, K., Bussmann-Holder, A., Górny, M., Szot, K., & Glazer, A.M. 2012. Precursor dynamics to the structural instability in $SrTiO_3$. *Phase Transitions*, **85**(11), 939–948. 62

Rondinelli, James M., & Fennie, Craig J. 2012. Octahedral rotation-induced ferroelectricity in cation ordered perovskites. *Advanced Materials*, **24**, 1961–1968. xiii, 7

Rotter, M., Mller, H., Gratz, E., Doerr, M., & Loewenhaupt, M. 1998. A miniature capacitance dilatometer for thermal expansion and magnetostriction. *Review of Scientific Instruments*, **69**(7). xiv, 24, 25

Rushchanskii, Konstantin Z., Spaldin, Nicola A., & Ležaić, Marjana. 2012. First-principles prediction of oxygen octahedral rotations in perovskite-structure $EuTiO_3$. *Phys. Rev. B*, **85**(Mar), 104109. 46

Sagarna, Leyre, Populoh, Sascha, Shkabko, Andrey, Eilertsen, James, Maegli, Alexandra E, Hauert, Roland, Schrade, Matthias, Karvonen, Lassi, & Weidenka,

Anke. 2014. In fl uence of the Oxygen Content on the Electronic Transport Properties of Sr_x Eu_{1-x} TiO_3 δ. 48

Sales, B. C., Chakoumakos, B. C., Jin, R., Thompson, J. R., & Mandrus, D. 2001. Structural, magnetic, thermal, and transport properties of $X_8Ga_{16}Ge_{30}$ ($X = \mathrm{Eu, Sr, Ba}$) single crystals. *Phys. Rev. B*, **63**(Jun), 245113. 39

Serrate, D., Teresa, J.M. De, Algarabel, P.A., Marquina, C., Morellon, L., Blasco, J., & Ibarra, M.R. 2005. Giant magnetostriction in Ca_2FeReO_6 double perovskite. *Journal of Magnetism and Magnetic Materials*, **290291, Part 2**(0), 843 – 845. Proceedings of the Joint European Magnetic Symposia (JEMS' 04). 67, 73

Serrate, D, Teresa, J M De, & Ibarra, M R. 2007. Double perovskites with ferromagnetism above room temperature. *Journal of Physics: Condensed Matter*, **19**(2), 023201. 3, 67

Shannon, R. D. 1976. Revised effective ionic radii and systematic studies of interatomic distances in halides and chalcogenides. *Acta Crystallographica Section A*, **32**(5), 751–767. 2, 5, 63

Shirane, G., & Yamada, Y. 1969. Lattice-Dynamical Study of the 110K Phase Transition in $SrTiO_3$. *Phys. Rev.*, **177**, 858–863. 46, 61

Siegel, Sidney, & Quimby, S. L. 1936. The Variation of Young's Modulus with Magnetization and Temperature in Nickel. *Phys. Rev.*, **49**(May), 663–670. 71

Sleight, A.W, & Weiher, J.F. 1972. Magnetic and electrical properties of Ba_2MReO_6 ordered perovskites. *J. Phys. Chem. Solids*, **33**(3), 679 – 687. 67, 68

Slonczewski, J. C., & Thomas, H. 1970. Interaction of Elastic Strain with the Structural Transition of Strontium Titanate. *Phys. Rev. B*, **1**(May), 3599–3608. 59, 60

Spaldin, Nicola A. 2003. *Magnetic Materials Fundamentals and Device Applications*. Cambridge University Press. xiii, 8

Spalek, Leszek J., Saxena, Siddharth S., Panagopoulos, Christos, Katsufuji, Takuro, Schiemer, Jason A., & Carpenter, Michael A. 2014. Elastic and anelastic relaxations associated with phase transitions in $EuTiO_3$. *Phys. Rev. B*, **90**(5), 054119. 47

Taylor, Publisher, Köhler, J, & Dinnebier, R. 2012. Phase Transitions : A Multinational Structural instability of $EuTiO_3$ from X- ray powder diffraction. 37–41. 46

Toby, Brian H. 2001. EXPGUI, a graphical user interface for GSAS. *Journal of Applied Crystallography*, **34**(2), 210–213. 48

Varshni, Y. P. 1970. Temperature Dependence of the Elastic Constants. *Phys. Rev. B*, **2**(Nov), 3952–3958. 31, 58, 69

Viallet, V., Marucco, J.-F., Saint, J., Herbst-Ghysel, M., & Dragoe, N. 2008. Structural, magnetic and electrical properties of a perovskite containing divalent europium $EuZrO_3$. *Journal of Alloys and Compounds*, **461**(12), 346 – 350. 35

Westerburg, W., Lang, O., Ritter, C., Felser, C., Tremel, W., & Jakob, G. 2002. Magnetic and structural properties of the double-perovskite Ca_2FeReO_6. *Solid State Communications*, **122**(34), 201 – 206. 67, 72

Yang, Yurong, Ren, Wei, Wang, Dawei, & Bellaiche, L. 2012. Understanding and Revisiting Properties of $EuTiO_3$ Bulk Material and Films from First Principles. *Phys. Rev. Lett.*, **109**(Dec), 267602. 46

Yoshii, K., Mizumaki, M., Nakamura, A., & Abe, H. 2003. Structure and magnetism of $Eu_{1-x}Dy_xTiO_3$. *Journal of Solid State Chemistry*, **171**, 345 – 348. 43

Zhandun, V. S., Zamkova, N. G., & Zinenko, V. I. 2015. Effect of an Eu3+ impurity on the antiferrodistortion and ferroelectric instabilities in an $EuTiO_3$ bulk crystal

and thin films. *Journal of Experimental and Theoretical Physics*, **120**(1), 103–109. 48

Zhou, J.-S., Goodenough, J. B., & Dabrowski, B. 2003. Transition from Curie-Weiss to enhanced Pauli paramagnetism in $R\mathrm{NiO}_3$ ($R = \mathrm{La}, \mathrm{Pr}, \ldots \mathrm{Gd}$). *Phys. Rev. B*, **67**(Jan), 020404. 35

Zong, Yanhua, Fujita, Koji, Akamatsu, Hirofumi, Murai, Shunsuke, & Tanaka, Katsuhisa. 2010. Antiferromagnetism of perovskite EuZrO_3. *Journal of Solid State Chemistry*, **183**(1), 168 – 172. 35

Zubkov, V.G., Tyutyunnik, A.P., Pereliaev, V.A., Shveikin, G.P., Khler, J., Kremer, R.K., Simon, A., & Svensson, G. 1995a. Synthesis and structural, magnetic and electrical characterisation of the reduced oxoniobates $\mathrm{BaNb}_8\mathrm{O}_{14}$, $\mathrm{EuNb}_8\mathrm{O}_{14}$, $\mathrm{Eu}_2\mathrm{Nb}_5\mathrm{O}_9$ and $\mathrm{Eu}_x\mathrm{NbO}_3$ ($x = 0.7,\ 1.0$). *Journal of Alloys and Compounds*, **226**(12), 24 – 30. 35

Zubkov, V.G., Tyutyunnik, A.P., Pereliaev, V.A., Shveikin, G.P., Khler, J., Kremer, R.K., Simon, A., & Svensson, G. 1995b. Synthesis and structural, magnetic and electrical characterisation of the reduced oxoniobates $\mathrm{BaNb}_8\mathrm{O}_{14}$, $\mathrm{EuNb}_8\mathrm{O}_{14}$, $\mathrm{Eu}_2\mathrm{Nb}_5\mathrm{O}_9$ and $\mathrm{Eu}_x\mathrm{NbO}_3$ ($x = 0.7,\ 1.0$). *Journal of Alloys and Compounds*, **226**(12), 24 – 30. 64

Appendix

List of publications

1. L. Li, J. R. Morris, M. R. Koehler, Z.-L. Dun, H. -D. Zhou, J. - Q. Yan, D. G. Mandrus, V. M. Keppens, *Structural and magnetic phase transitions in* $EuTi_{1-x}Nb_xO_3$, arXiv:1505.05528, accepted, Phys. Rev. B (2015).

2. A.A. Aczel, L. Li, V.O. Garlea, J.-Q. Yan, F. Weickert, V.S. Zapf, M. Jaime, P.J. Baker, V. Keppens, and D. Mandrus, *Spin liquid ground state in the frustrated J1-J2 zigzag chain system* $BaTb_2O_4$, accepted, Phys. Rev. B(R) (2015).

3. L. Li, M. R. Koehler, I. Bredeson, J. He, D. Mandrus, and V. Keppens, *Magnetoelastic coupling in* A_2FeReO_6 *(A = Ba and Ca) probed by elastic constants and magnetostriction measurements*, J. Appl. Phys. **117**, 213913 (2015).

4. D. S. Parker, N. Ghimire, J. Singleton, J. D. Thompson, E. D. Bauer, R. Baumbach, D. Mandrus, L. Li, and D. J. Singh, *Magnetocrystalline anisotropy in UMn2Ge2 and related Mn-based actinide ferromagnets*, Phys. Rev. B **91**, 174401 (2015).

5. D. Braam, C. Gomez, S. Tezok, E.V.L. de Mello, L. Li, D. Mandrus, Hae-Young Kee, J.E. Sonier, *Magnetic properties of the helimagnetic* $Cr_{1/3}NbS_2$ *observed by* μSR, Phys. Rev. B **91**, 144407 (2015).

6. L. Li, H. D. Zhou, J.-Q. Yan, D. Mandrus and V. Keppens, *Magnetic phase diagram of* $EuTi_{1-x}B_xO_3$ *(B=Zr, Nb)*, APL Materials **2**, 110701 (2014).

7. A. A. Aczel, L. Li, V. O. Garlea, J.-Q. Yan, F. Weickert, M. Jaime, B. Maiorov, R. Movshovich, L. Civale, V. Keppens, D. Mandrus, *Magnetic ordering in the frustrated J1-J2 Ising chain candidate* $BaNd_2O_4$, Phys. Rev. B **90**, 134403 (2014).

8. A. A. Aczel, D. E. Bugaris, L. Li, J.-Q. Yan, C. de la Cruz, H.-C. zur Loye, and S. E. Nagler, *Frustration by Competing Interactions in the Highly-distorted Double Perovskites* La_2NaBO_6 *(B = Ru, Os)*, Phys. Rev. B **87**, 014435 (2013).

9. T. Li, A. Patz, P. Lingos, L. Mouchliadis, L. Li, J. Yan, I. E. Perakis, J. Wang, *Correlating Quasi-Electron Relaxation with Quantum Femtosecond Magnetism in the Order Parameter Dynamics of Insulating Manganites*, arXiv:1409.1591, under review (2015).

10. A. Banerjee, C.A. Bridges, J-Q. Yan, A.A. Aczel, L. Li, M.B. Stone, G.E. Granroth, M.D. Lumsden, Y. Yiu, J. Knolle, D.L. Kovrizhin, S. Bhattacharjee, R. Moessner, D.A. Tennant, D.G. Mandrus, S.E. Nagler, *Proximate Kitaev Quantum Spin Liquid Behavior in* α-$RuCl_3$, arXiv:1504.08037, under review (2015).

Vita

Ling Li was born to Longhua Li and Ling He in Xiema County, Chongqing City in southwestern part of China. She attended High School Affiliated to Southwest University from 2000 to 2006. Ling obtained her B. S. in Materials Science and Engineering (MSE) from University of Science and Technology Beijing, China in July 2010. She started graduate school majoring in MSE at The University of Tennessee in August 2010. She received her M.S. in December 2013 and Ph.D. in August 2015, both in MSE. Her thesis is focused on crystal growth and physical properties of complex perovskite oxides with strong coupling between structural, magnetic, and electrical degrees of freedom. Besides her thesis projects, she also collaborated with other scientists on multiple projects including the frustrated J1-J2 zigzag chain system $BaNd_2O_4$ and $BaTb_2O_4$, the chiral magnetic system $Cr_{1/3}NbS_2$, proximate Kitaev quantum spin liquid system α-$RuCl_3$, and giant magnetocaloric effect in $DyVO_3$, *etc.*